Significance of brittle deformation in the footwall of the Alpine Fault, New Zealand: Smithy Creek Fault zone

J.-E. Lund Snee [a,*,1], V.G. Toy [a], K. Gessner [b]

[a] Geology Department, University of Otago, PO Box 56, Dunedin 9016, New Zealand
[b] Western Australian Geothermal Centre of Excellence, The University of Western Australia, 35 Stirling Highway, Crawley, WA 6009, Australia

ABSTRACT

The Smithy Creek Fault represents a rare exposure of a brittle fault zone within Australian Plate rocks that constitute the footwall of the Alpine Fault zone in Westland, New Zealand. Outcrop mapping and paleostress analysis of the Smithy Creek Fault were conducted to characterize deformation and mineralization in the footwall of the nearby Alpine Fault, and the timing of these processes relative to the modern tectonic regime. While unfavorably oriented, the dextral oblique Smithy Creek thrust has kinematics compatible with slip in the current stress regime and offsets a basement unconformity beneath Holocene glaciofluvial sediments. A greater than 100 m wide damage zone and more than 8 m wide, extensively fractured fault core are consistent with total displacement on the kilometer scale. Based on our observations we propose that an asymmetric damage zone containing quartz–carbonate –chlorite–epidote veins is focused in the footwall. Damage zone asymmetry likely resulted from the fact that the hanging wall was mostly deformed at greater depth than the footwall, rather than resulting from material contrasts across the fault plane. Kinematic inversions on mineralized fractures within the damage zone suggest veins formed in the current stress regime, from fluids comparable to those now circulating in the footwall. The Smithy Creek Fault zone is therefore a rare exhumed example of the modern footwall hydrothermal system, and of a structure actively accommodating footwall deformation near the Alpine Fault zone. Two significantly less mature, subvertical faults having narrow (20 cm or less) damage zones and similar orientations to nearby strike-slip segments of the Alpine Fault crosscut the mineralized zone at Smithy Creek. We envisage that hydrothermal mineralization strengthened the fault core, causing it to widen as later slip was partitioned into the (now) weaker surrounding damage zone. With progressive alteration, formation of favorably oriented faults became preferable to reactivation of the existing structure.

© 2013 Elsevier Ltd. All rights reserved.

1. Introduction

Little is known about the role of brittle deformation in the footwall of the dextral oblique Alpine Fault zone, New Zealand. Crustal deformation is often localized into shear zones, which are differentiated into ductile, brittle-ductile, and brittle (fault) types (Sibson, 1977; Ramsay, 1980). A common fault structure model comprises a fault core (the region that has accumulated the most displacement), containing cataclasites, gouge, and breccia (Chester & Logan, 1987; Chester et al., 1993; Caine et al., 1996; Rawling et al., 2001; Faulkner et al., 2006; Meneghini & Moore, 2007; Mitchell & Faulkner, 2009). A damage zone surrounding the fault core is composed of mechanically associated structures, which can include fractures, veins, folds, and smaller faults (Caine et al., 1996; Rawling et al., 2001; Faulkner et al., 2006, 2010; Meneghini & Moore, 2007; Mitchell & Faulkner, 2009). The mechanical and hydraulic properties of the surrounding host rock are typically not related to the fault in question (Caine et al., 1996; Rawling et al., 2001; Mitchell & Faulkner, 2009). Natural examples are more complex than this simple model, displaying heterogeneity both parallel and perpendicular to the fault plane (cf. Wibberley et al., 2008; Faulkner et al., 2010; Mitchell et al., 2011).

Fault zone structure is significantly influenced by stress regime, amount of displacement, fault zone geometry and subsidiary

* Corresponding author. Tel.: +1 720 289 8972.
  E-mail address: lundsnee@stanford.edu (J.-E. Lund Snee).
[1] Present address: Department of Geological and Environmental Sciences, Stanford University, Braun Geology Corner, Building 320, 450 Serra Mall, Stanford, CA 94305, USA.

structures, depth and temperature, characteristics of the host rock (particularly pre-existing fractures, lithological contacts, or other anisotropy), and evolution with time of all of these parameters (Caine et al., 1996; Kassem & Ring, 2004; Wibberley et al., 2008). Fault zone permeability influences hydrocarbon and precious metal formation and trapping, as well as earthquake behavior (Wibberley et al., 2008; Faulkner et al., 2010).

Many questions remain about the evolution of fault zone structure, as well as the temporal evolution of fluid flow and permeability within and between the various structural components (Faulkner et al., 2010). Fault cores are usually less permeable than surrounding damage zones (Caine et al., 1996; Micarelli et al., 2006; Sutherland et al., 2012). Damage zone and core width and the extent of mineralization influence overall fault zone permeability and permeability structure. This is partly due to significantly lower fracture density in the fault core, but field and experimental data also reveal that the comminuted, fine-grained cataclasites and gouges common in fault cores typically have low permeabilities, especially when phyllosilicate content is high (Caine et al., 1996; Micarelli et al., 2006; Wibberley & Shimamoto, 2003; Wibberley et al., 2008). However, some fault cores also act as fluid conduits and damage zones, if mineralized, can act as fluid barriers (Caine et al., 1996).

In addition, varying fault zone protoliths result in heterogenous structure and permeability (Wibberley & Shimamoto, 2003; Micarelli et al., 2006). Fault core and damage zone permeabilities are typically anisotropic, with across-fault and fault-parallel permeability controlled by complex factors including phyllosilicate content and preferred orientation, connectivity of permeable and non-permeable zones (such as slip surfaces), mineralization, and orientation of fractures with respect to the prevailing stress state (Faulkner et al., 2010; Sutherland et al., 2012).

Fault zone research has focused especially on strike-slip fault zones (e.g. Chester & Chester, 1998; Wibberley & Shimamoto, 2003; Dor et al., 2006; Faulkner et al., 2006, 2008; Boutareaud et al., 2008; Finzi et al., 2009; Mitchell et al., 2011), but less is known about the processes occurring during evolution of relatively complex oblique-thrust faults, where material moves in P-T-t space during deformation. In the transpressive Alpine Fault zone, a >50 m zone of phyllosilicate and carbonate alteration is superimposed on the principal slip surface and its surroundings, contributing to a c. 10^6 reduction of permeability within this zone (particularly nearest the principal slip zone) that is thought to generate episodic development of a pressure gradient across the fault which in turn facilitates seismic slip (Sutherland et al., 2012).

Recent road works have exposed a spectacular segment of the Smithy Creek Fault in Australian Plate rocks ∼1.5 km W of New Zealand's Alpine Fault, and enable detailed investigation of its internal structure and kinematics. We have investigated the structural and permeability history of the fault zone and herein contribute to the understanding of fault zone heterogeneity a scaled, schematic section roughly normal to the principal slip surface of this structure. We describe centimeter-scale features across the section that document hydrologic and structural characteristics across the most damaged part of the fault zone at high spatial resolution.

The Smithy Creek Fault provides insights into the questions considered above and the nature of deformation in the footwall of this complex plate boundary system. Small faults and other structures within the asymmetrical Smithy Creek Fault zone also record a varied history of strain and mineralization over the lifespan of the fault zone. The study area exposes relatively young faults that crosscut a more evolved, differently oriented structure, but both sets of faults are thought to be associated with the same long-lived

plate boundary kinematic and hydrothermal system. This provides an excellent opportunity to study the evolution of structural and fluid flow characteristics of the footwall of an active, crustal-scale oblique thrust, including whether, and how, the kinematics, timing, and style of brittle and ductile structures at multiple scales in this footwall fault zone were influenced by broader-scale plate boundary processes.

Characterization of smaller faults surrounding major fault zones, such as the one we describe herein, contributes to better understanding of strain partitioning, energy budget, and earthquake processes. The portion of the Alpine Fault near the study area, for example, has experienced large (≥250 km along strike, M7.5–7.9 or greater) seismic ruptures every ∼200–300 years, with the next major event likely to be imminent (Adams, 1980; Sutherland et al., 2007; Berryman et al., 2012; De Pascale & Langridge, 2012; Howarth et al., 2012).

2. Geologic setting

The Alpine Fault zone (AFZ), a major NE–SW-striking active shear zone in the South Island of New Zealand, forms the major part of the complex margin system between the Australian and Pacific plates in this area, dextrally displacing basement terranes by up to 460 km (Sutherland et al., 2000). The fault accommodates right-lateral oblique-thrust slip in response to an oblique Pacific–Australian plate convergence vector (Walcott, 1978; DeMets et al., 1994; Sutherland et al., 2006). Convergence has resulted in rapid uplift and erosion of the Southern Alps, whose northwestern range front coincides with the fault trace (Walcott, 1998).

The AFZ has been divided into three zones, each having differing structural characteristics and accommodating varying amounts of plate displacement (e.g. Anderson et al., 1993; Craw & Campbell, 2004). North of Arthur's Pass, relative plate motion is partitioned onto several strike-slip structures in the Marlborough Fault System (Fig. 1), as well as reverse faults in the Buller region to the northwest of the Alpine Fault (Anderson et al., 1993; Cooper & Norris, 1994; Norris & Cooper, 2001). In the central section, between Haast and Arthur's Pass, the AFZ accommodates ∼60–75% of the component of relative plate motion parallel to it (35.5 ± 1.5 mm yr^{-1}; Norris & Cooper, 2001; Norris & Cooper, 2007). The central AFZ accommodates varying amounts of the 10 mm yr^{-1} average convergent component of plate boundary motion, with AFZ dip-slip rates reaching highs of ∼6–9 mm yr^{-1} at the Franz Josef glacier (Norris & Cooper, 2001; Little et al., 2005). The southern section, south of Haast, is subvertical (dipping 70–90°) and accommodates 55–85% of plate displacement (Sutherland et al., 2000). Slip is also partitioned onto faults up to 300 km southeast of the Alpine Fault (Sutherland et al., 2000). Further south the AFZ links into the Puysegur oceanic subduction zone (Anderson et al., 1993; Leitner et al., 2001; Norris & Cooper, 2007).

Based on geodetic inversion, the Alpine Fault is thought to be fully locked to a depth of ∼12 km in the vicinity of the study area (central zone), with continuous steady state creep occurring beneath ∼18 km (Pearson et al., 2000; Beavan et al., 2007). An area of low seismicity on the Alpine Fault near Franz Josef Glacier, immediately southeast of the study area, is interpreted to reflect nearly total fault zone locking at seismogenic depths (Evison, 1971; Beavan & Haines, 2001; Sutherland et al., 2007).

The central Alpine Fault strikes 055° at 10^6–10^4 m scale but is locally partitioned at depths less than 4 km into smaller oblique thrusts that commonly strike 020°–050° and dip southeast at ∼30°, and right-lateral strike-slip faults that strike 070°–090° (Norris & Cooper, 1995, 1997, 2001). LiDAR (light detection and
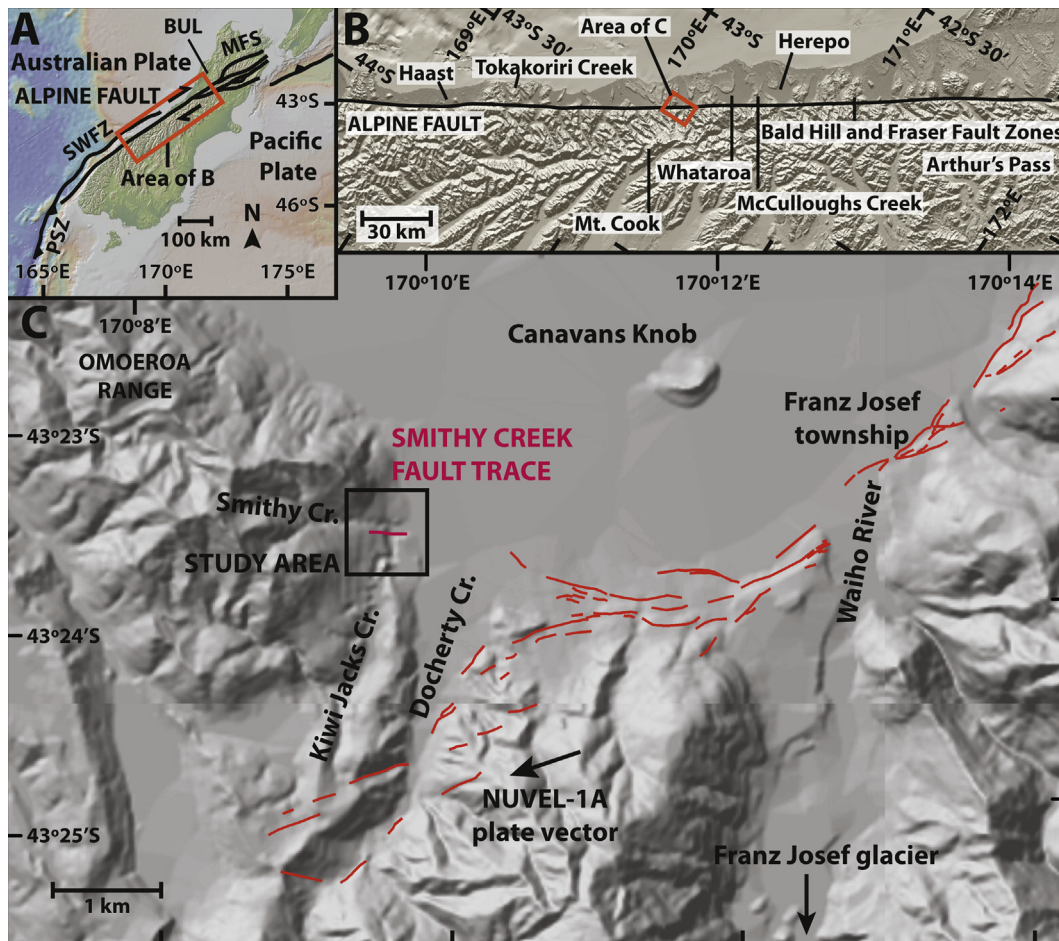
Fig. 1. (A) Map of the South Island, New Zealand displaying the Global Multi-Resolution Topography (GMRT) synthesis (Ryan et al., 2009) basemap, generated in GeoMapApp (Haxby et al., 2010). Box indicates vicinity of study area. Fault trace locations after Sutherland et al. (2006). Abbreviations: BUL—Buller region; MFS—Marlborough Fault System; PSZ—Puysegur oceanic subduction zone; SWFZ—South Westland Fault Zone. (B) Enlargement of the central South Island with approximate Alpine Fault trace shown. Basemap is the same as in (A). (C) Enlargement of the Franz Josef–Whataroa area, showing the Alpine Fault and Nuvel-1A plate vector from DeMets et al. (1994) and third-order (10^3–10^0 m) fault traces associated with the central Alpine Fault from LiDAR data (after Barth et al., 2012).

ranging) data collected over the Alpine Fault trace indicate that partitioning on the Alpine Fault occurs also at two finer scales; at the 10^4–10^3 m scale it is partitioned into dextral strike-slip and dextral oblique-thrust segments. At the 10^3–10^0 m scale the Alpine Fault is partitioned into dextral strike-slip segments with connecting oblique normal and thrust segments, as well as aligned anticlinal ridges, reflecting the likely existence of flower structures in the hanging wall at shallow depth (Barth et al., 2012). Seismic reflection profiles, thermal modeling, thermochronology, and field observations suggest segments converge at depth into a single ductile shear zone that accommodates oblique-thrust movement, which strikes ~055°, dips ~45° to the southeast, and extends to a depth of 30–35 km (Davey et al., 1995; Norris & Cooper, 1995; Sutherland et al., 2000; Little et al., 2005; Toy et al., 2008).

The Smithy Creek Fault is exposed ~1.5 km W of a group of 10^4–10^3 m scale, right-lateral oblique thrusts of the Alpine Fault striking 040–045/30 SE. To the west of Docherty Creek the thrusts transition to a zone of primarily strike-slip faults characterized by narrow (<1 m), subvertical clay gouge zones striking 065–090° (Norris & Cooper, 1995, 1997). Between Docherty and McCulloughs creeks, dextral 10^3–10^0 m scale strike-slip segments of the Alpine Fault strike predominantly 70–75°, are subvertical, and have orientations independent of topography (Table 1; Fig. 1). LiDAR coverage of

the Alpine Fault trace ends ~0.75 km from the study area but this relative proximity allows us to relate the Smithy Creek Fault to the Alpine Fault.

2.1. Alpine Fault footwall structure and rheology

Components of plate boundary displacement that are not accommodated by the AFZ are partitioned onto faults in the hanging wall (Pacific Plate), in a zone extending up to 200 km SE (Walcott, 1978; Norris et al., 1990; Little et al., 2002; Sutherland et al., 2006). Geodetic surveys indicate that a small component of contemporary elastic deformation is partitioned into the Australian

Table 1
Orientations of faults associated with the central Alpine Fault, with strikes obtained from LiDAR and dips obtained from field observations (from Barth et al., 2012).

	Orientation of fault plane (strike/dip)	Orientation of slip vector (plunge → trend)
Major thrust segments; near surface	040°–045°/30°SE	15° → 071°
Major reverse segments at greater depths	040°–045°/50°SE	30° → 071°
Major strike-slip segments	070°–075°/90°	15° → 071°
Oblique segments	060°–065°/60°SE	15° → 071°

Plate slightly west of the Alpine Fault (Beavan & Haines, 2001; Beavan et al., 2007). Any consequences of this strain build-up for footwall fault rupture are not known. The nature and extent of footwall deformation in the central segment of the AFZ between Arthur's Pass and Haast is not well understood because of both the dearth of historical earthquake epicenters west of the AFZ, particularly in the central zone (e.g. Anderson et al., 1993; Leitner et al., 2001), and sparse exposure of Western Province basement (e.g. Adams, 1975; Cooper & Tulloch, 1992; Ireland, 1992; Cooper & Norris, 1994; Adams, 2004). Potentially Tertiary-active footwall structures include the South Westland Fault Zone, which is sub-parallel to the Alpine Fault but is not known for certain to be active (Sutherland, 1996; Sutherland et al., 2000, 2006; Norris & Cooper, 2001); the Fraser and Bald Hill Range faults (e.g. Rattenbury, 1991; Kamp et al., 1992); and smaller structures at the west coast near Tokakoriri Creek (Phillips et al., 2005).

2.2. Smithy Creek lithologies

Herein we describe faulted rocks that crop out in the Omoeroa Range, near Smithy, Kiwi Jacks, and Docherty creeks, south Westland, New Zealand (Fig. 1). The (here named) Smithy Creek Fault is a dextral oblique thrust that cuts a calc-alkaline biotite–hornblende–two-pyroxene monzonite–monzodiorite pluton (with no clear geochemical or temporal affinity with any formal nearby plutonic suites) and assorted igneous intrusions at a roadcut on State Highway 6 near Smithy Creek and in Kiwi Jacks Creek nearby (Cox & Barrell, 2007; Tulloch et al., 2009). This pluton has a U–Pb chemical abrasion thermal ion mass spectrometry (CA-TIMS) zircon age of 100.94 ± 0.15 Ma, dissimilar to most ages (230–105 Ma) derived from the Median Batholith (Tulloch et al., 2009). Instead, this age suggests it is related to a NZ-wide episode of volcanism c. 101 Ma associated with Gondwana breakup (Tulloch et al., 2009). A lamprophyre dike at Canavans Knob returned an Oligocene whole rock K–Ar age of 32.5 ± 0.8 Ma, but this might reflect the timing of exhumation (Nathan et al., 2000). In the immediate study area, a 2.6 ± 0.6 Ma age of apatite annealing (exhumation from ∼3 km) was obtained from fission-track dating on a hornfels sample from the Western Province basement (Seward & Nathan, 1990). Apatite fission-track dating conducted at nearby Canavan's Knob revealed exhumation to less than 3 km depth by 1.4 ± 0.8 Ma (Seward & Nathan, 1990).

3. Methods

3.1. Field techniques

Representative lithologies are described based on field examination and oriented thin sections. Orientations of veins, fractures, and slickensides were measured using a hand compass, and orientations of veins, fractures, and planar intrusions were also obtained from photogrammetric data using SiroVision v.4.1 (CSIRO, 2010). Planar data are given as strike, dip, and dip direction, and linear data are given as plunge and trend. Orientation data collected by compass were not combined with data obtained from photogrammetry to avoid redundant measurements.

3.2. Close-range digital photogrammetric analysis of discontinuity data

3-D composite images were generated from eight stereopairs of digital photographs for the Smithy Creek Fault road outcrop on State Highway 6 (NZTM coordinates 1367545 E, 5191633 N; Fig. 2). Each stereophoto pair was taken at a different location, facing
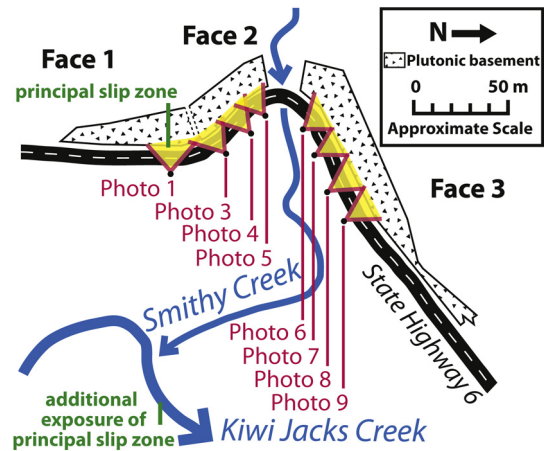

Fig. 2. Schematic outcrop diagram showing the location of the 'principal slip zone' of the Smithy Creek Fault, digital stereophoto locations, and approximate extent of un-differentiated Western Province plutonic rocks in the study area. Each photo represents two camera locations, separated at an outcrop-parallel distance of ∼1/8 the distance from the cameras to the outcrop.

toward most of the outcrop, and most images overlap slightly (Fig. 3). "Approach A" of Sturzenegger and Stead (2009) was employed; digital photographs were taken using a Canon EOS 5D with a 28 mm lens placed on tripods at two different locations spaced ∼1/8 of the distance between these cameras and the outcrop. A compass and laser rangefinder with built-in digital clinometer were used to survey the distances, slope, and azimuth between tripod locations and from both tripods to each of two control points on the outcrop face. The two control points were chosen for their locations on the left and right thirds of the camera fields-of-view. Separate stereopairs were collected for each of eight different locations covering most of the Smithy Creek portion of the study area. Orientations of fractures, veins, and other planar structures were picked manually (without using automatic joint detection algorithms) from the 3-D images. Photogrammetry does not allow differentiation between discontinuities that have and have not accommodated shear, and slick-enside lineation data are not easily collected using this method. Digital stereophoto analysis usually detects larger features, such as dikes and larger joint surfaces, whereas in this study hand measurements are generally of smaller fractures and mineralized veins closer to ground level.

3-D photogrammetric analysis is known to produce highly accurate data for orientation, spacing, and location of surfaces, with close agreement observed between hand-measured and digitally obtained surfaces, provided that ideal surveying and field techniques are employed and that cameras and lenses are well suited to the purpose and are situated at an appropriate distance and angle to the outcrop (Haneberg, 2008; Sturzenegger & Stead, 2009). However, various biases can be introduced into such discontinuity datasets (e.g. Terzaghi, 1965; Sturzenegger & Stead, 2009; Lato et al., 2010). The discontinuity data obtained from the photogrammetric measurements were tested for bias by plotting poles to discontinuities measured in each photopair on equal-area lower hemisphere projection stereonets together with the estimated average outcrop face orientation. The locations of clusters of poles to discontinuities from each photopair were found to vary with changing outcrop face orientation and to systematically relate to the orientation (Fig. 4), suggesting that the photogrammetric data might suffer from orientation bias. A weighting factor was applied to contoured data to account for possible trace exposure bias using the Terzaghi (1965) method (Fig. 5). Appendix A discusses the methodology of this correction factor and considers other possible
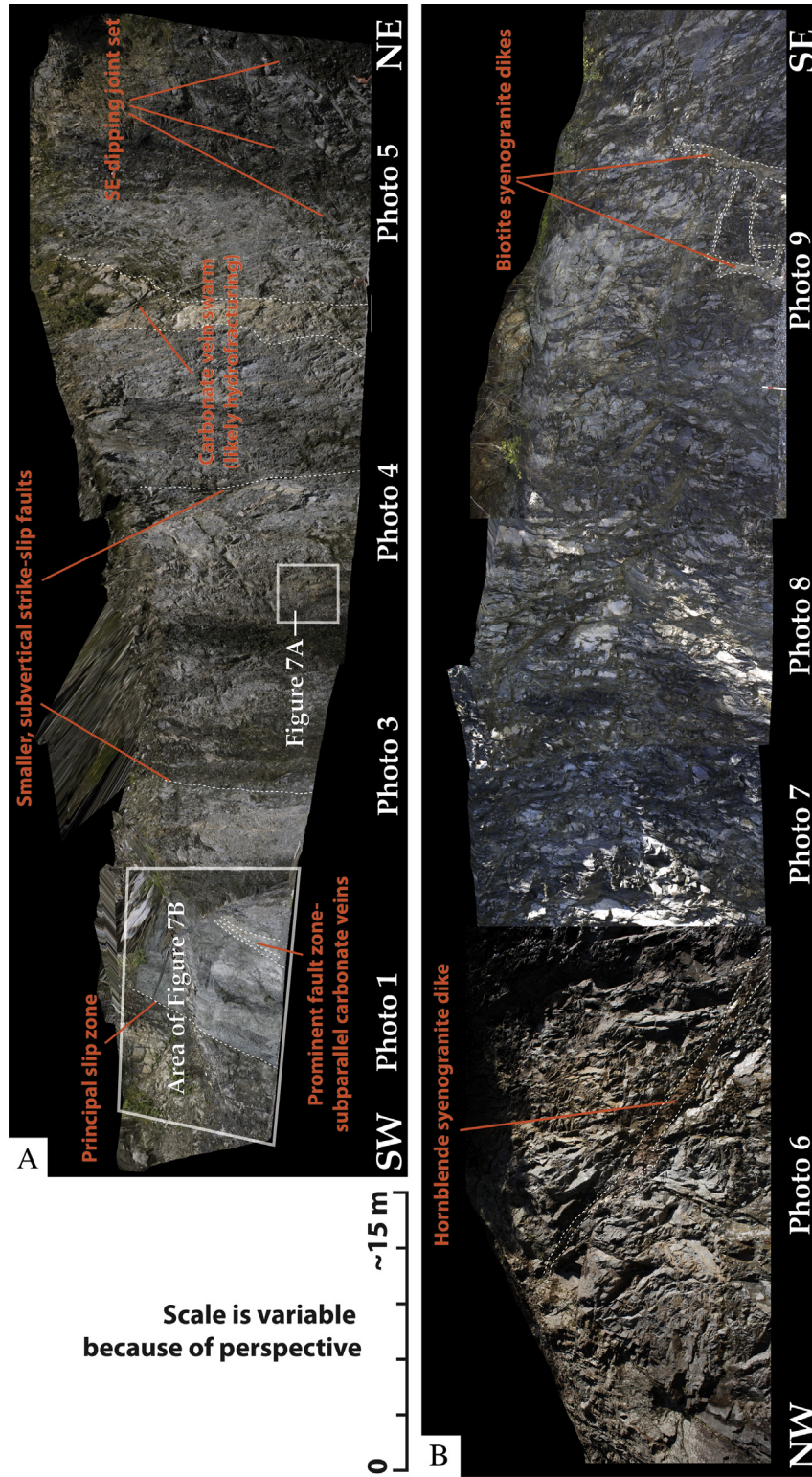
Fig. 3. Mosaic of digital stereophotos of an exposure of the Smithy Creek Fault at State Highway 6. Scale varies across outcrops because of the image perspective. (A) Faces 1 and 2, south of Smithy Creek. (B) Face 3, north of Smithy Creek.

biases that might affect these data. However, the uncorrected data were found to accord well with uncorrected hand compass-measured discontinuity data, so the Terzaghi (1965) correction is considered unnecessary (Section 4.2) but it is displayed here for comparison purposes.

3.3. Aleksandrowski (1985) method

The Aleksandrowski (1985) method allows determination of possible orientations of principal stresses (i.e. principal elastic strain axes) acting during a single episode of faulting in anisotropic
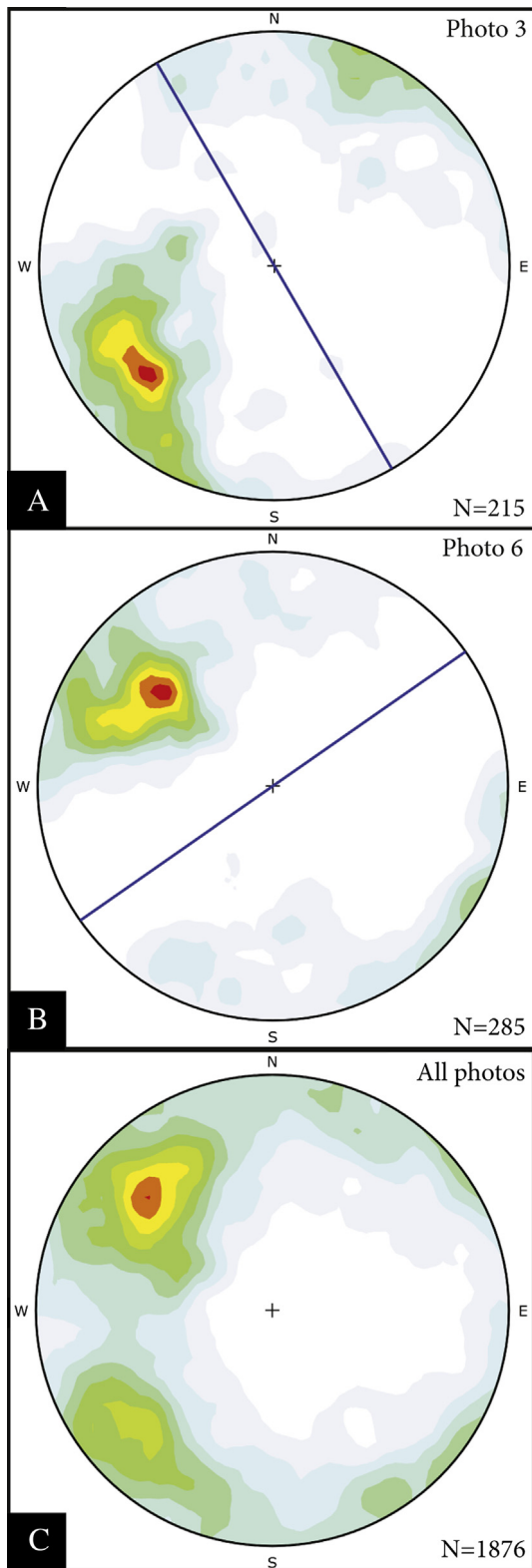
Fig. 4. (A) and (B) Stereoplots of poles to discontinuities by for photo locations 3 and 6 (locations indicated in Figs. 2 and 3), and (C) the combined data for all photo locations. Great circles represent average outcrop orientations. Fisher et al. (1987) contouring is uncorrected for orientation bias.

rocks. These orientations are determined by plotting the great circles connecting lineation points and the poles to the fracture surface planes (*M*-planes), as well as the poles to these *M*-planes (*πM*-points) on stereonets (Aleksandrowski, 1985). Lineation and fracture data were measured by hand compass. *M*-planes will intersect at several common intersection points (CIPs; Appendix B). For each CIP, a best-fit great circle is then constructed containing the poles to these intersecting *M*-planes (GCP) and another best-fit great circle is constructed between the slickenside lineations associated with the same *M*-planes (GCF); these two great circles should intersect at one of the principal elastic strain axes. This method does not distinguish between the principal stress axes (i.e. S_1, S_2, and S_3), so this must be inferred from other data, such as microstructural shear sense indicators, if possible.

3.4. Relative fault zone maturity

We consider fault zone maturity in relative terms. A relatively 'mature' fault zone has some or all of the following characteristics: (1) greater damage zone and fault core thickness, (2) a more planar principal slip zone, (3) greater complexity within the damage zone and fault core, (4) finer overall, or a greater proportion of small particles (indicating more extensive comminution), and (5) more pervasive alteration. Damage zone and fault core width are especially important to evaluating maturity because displacement and overall fault zone width are positively correlated in many natural examples (e.g. Sagy et al., 2007; Rockwell & Ben-Zion, 2007; reviews in Wibberley et al., 2008; Faulkner et al., 2010). Ferrill et al. (2008) argued that fault zone thickness is established early, at initial propagation, and that during later slip the slip surface narrows but fault zone damage intensifies within existing boundaries. However, in some studies the thickness of the gouge zone within a fault core increases with total displacement (Sagy & Brodsky, 2009). Competing processes must thus control damage zone, fault core, and gouge zone widths. For example, localization of deformation in the gouge zone inside the fault core may inhibit outer damage zone growth (Micarelli et al., 2006), but further slip may also weaken the protolith and more surrounding rock tends to be incorporated into the outer damage zone during slip (Wibberley et al., 2008). Fault core cataclasites start to develop at 1–5 m of fault displacement (Sagy & Brodsky, 2009).

4. Fault zone characterization

4.1. Qualitative description of fault zone

The Smithy Creek Fault is exposed at two locations (Figs. 1 and 2): (1) at the south side of Kiwi Jacks Creek near its confluence with Smithy Creek (as identified by Wooding, 1984), and (2) approximately 250 m W at a roadcut along State Highway 6 at Smithy Creek (Fig. 3), where an asymmetrical, >8 m wide fault core is exposed (<0–6.2 m on measured section, Fig. 6). The damage zone and fault core at the Kiwi Jacks Creek exposure have comparable size and degree of damage to the Smithy Creek roadcut locality (although the damage zone and fault core are not fully exposed at Kiwi Jacks Creek) and the principal slip zone is oriented 089/64 S, which is nearly identical to the remarkably planar slip zone at the Smithy Creek locality (090/70 S), suggesting that the two structures are continuous or closely linked. Descriptions below refer to the roadcut locality unless indicated otherwise because of its better exposure, but the two localities are very similar.

The Smithy Creek Fault principal slip zone (0.55–0.6 m on log) is composed of ultracataclasite (fault rock classification after Sibson,
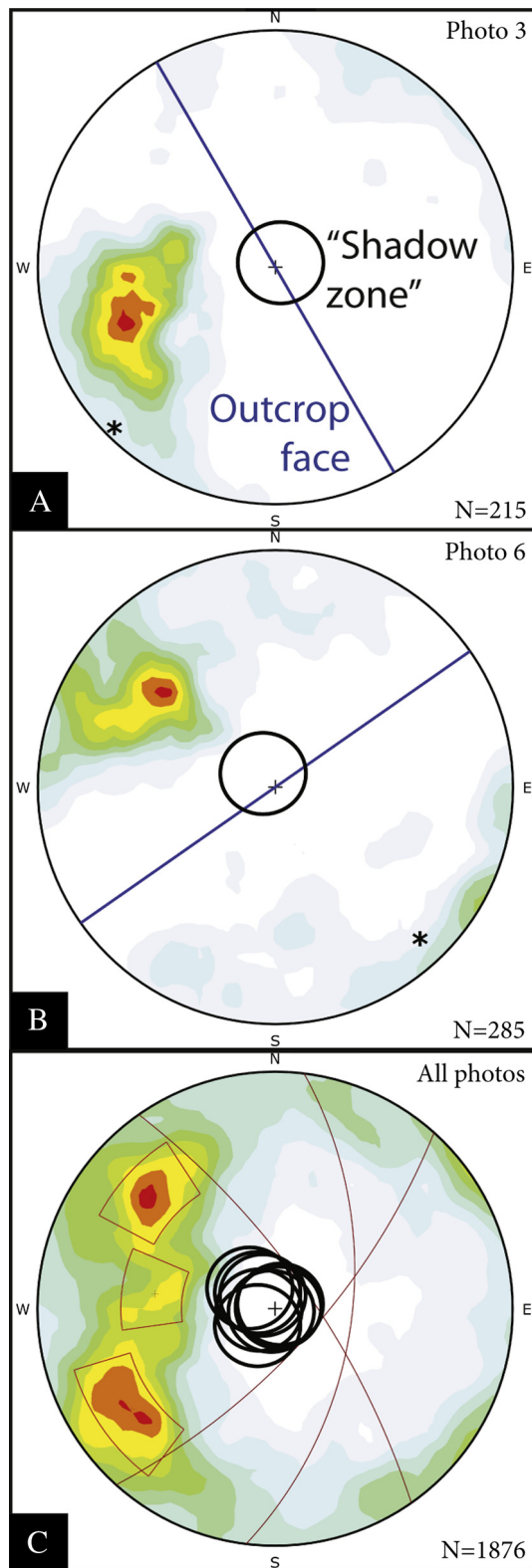
Fig. 5. (A) and (B) Stereoplots of poles to discontinuities calculated from photogrammetry for photo locations 3 and 6, with Fisher et al. (1987) contouring corrected for orientation bias by the Terzaghi (1965) method. Great circles represent average outcrop orientations. Black areas are expected "shadow zones" (Brideau et al., 2012) due to occlusion related to approximate camera line-of-sight (black asterisk). (C) Corrected photogrammetric discontinuity data pooled from all photos, with shadow zones from all photopairs shown in black and main clusters of poles indicated in red sectors. Red great circles represent the planes for the centers of the clusters. The uncorrected photogrammetry data were found to accord well with uncorrected data

1977), with slickenlines oriented ∼31/103 (Fig. 6B). A clay gouge horizon is in the footwall side of the principal slip zone. These structures occur within a more than 8 m wide fault core. The fault core hanging wall contains indurated, weakly foliated ultra-cataclasites with sparse subvertical carbonate veins. The fault core footwall (0.6−6 m in log) is composed of foliated protocataclasite to cataclasite less indurated than the hanging wall and containing anatomizing 1−5 mm thick clay gouge zones, mineralized veins, and protolith clasts. These constituents together define an anastomosing but overall fairly consistent foliation (071/77 S) in the clay to fine sand cataclasite matrix that is slightly oblique (subtending an angle of ∼19°) to the principal slip zone. Relatively undeformed clasts of protolith are abundant in the footwall, and are commonly bound by branching clay horizons that are subparallel to internal foliation. Average clast size increases away from the principal slip surface, from <1 mm to 2 cm (1 mm on average) within 20 cm of the principal slip surface, to coherent phacoids of the plutonic protolith and intrusions <15 cm long at the boundary with the surrounding damage zone. Foliation in the hanging wall, where present, ranges from parallel with, to oblique to, the principal slip surface. The hanging wall fault core has undergone significant grain size reduction, with >90% of the rock affected.

Two narrow, smaller, subvertical, brittle structures are exposed in the footwall damage zone of the main fault (Fig. 3). In places, these structures, which contain 3−12 mm of laminated clay gouge, have their own ≤20 cm thick surrounding zone of rock more damaged than the rest of the outcrop, indicating these features are small faults. They contain little or no cataclasite and no slickensides are preserved, but their subvertical orientations suggest strike-slip faults according to the principals of Anderson (1951). These faults are considered significantly less mature (Section 3.4) than the main oblique structure because their damage zones are nearly 10^3 narrower than the main structure, and because the degree of mineralization within these faults is not appreciably higher than that of the surrounding Smithy Creek Fault damage zone, and is significantly lower than the Smithy Creek Fault core.

4.1.1. Lithologies in fault zone

The oldest and most voluminous lithology in the study area is biotite−hornblende−two-pyroxene monzonite−monzodiorite, which is intruded by granitoids and lamprophyres (Fig. 7A). Multiple intrusive protoliths have been incorporated into the fault zone from the adjacent rock. Near Smithy Creek, the fault core (<0−6.2 m on log; Fig. 7B and C) primarily comprises cataclastic porphyritic hornblende−pyroxene quartz diorite and altered white-green granitoid (Fig. 8A) that resembles a nearby chloritized hornblende−biotite monzogranite. Multiple additional intrusive compositions, ranging from syenogranite to monzogranite and lamprophyre (Fig. 8B and C), are exposed in the damage zone but are not observed in the fault core. Although the fault core comprises only minor amounts of the host pluton protolith near Smithy Creek, cutting instead younger intrusions, it cuts the pluton at the exposure in Kiwi Jacks Creek, ∼200 m to the east (Wooding, 1984).

4.1.2. Sense of shear

The fault is interpreted to have most recently experienced oblique reverse motion, based on slickensides, mesostructures in

measured by hand compass (Section 4.2), so the Terzaghi (1965) correction may be unnecessary despite the observation that discontinuity orientations vary with outcrop face orientation (Fig. 4). The corrected data are shown here for comparison purposes. (For interpretation of the references to color in this figure legend, the reader is referred to the web version of this article.)
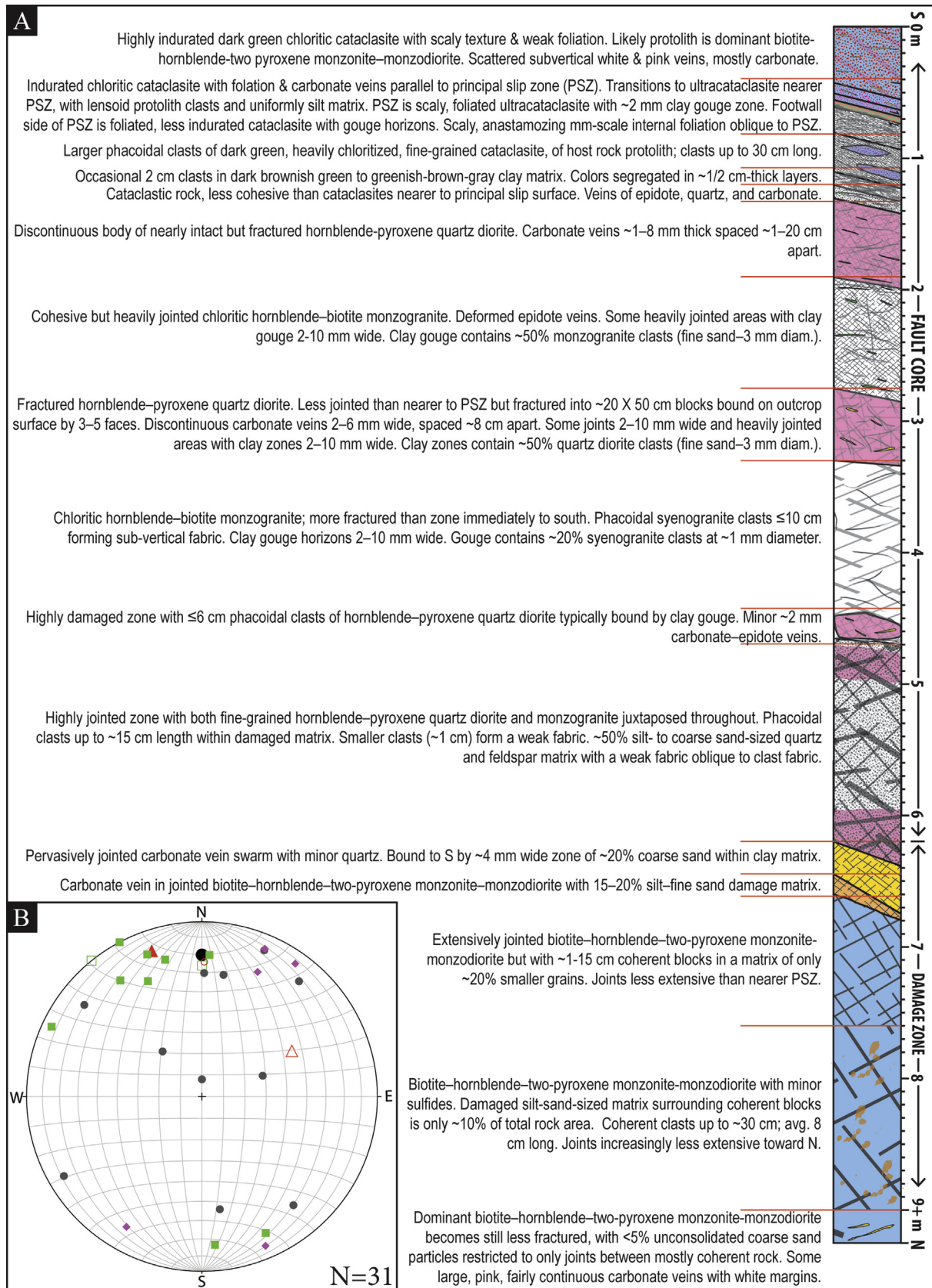
A

Highly indurated dark green chloritic cataclasite with scaly texture & weak foliation. Likely protolith is dominant biotite-hornblende-two pyroxene monzonite–monzodiorite. Scattered subvertical white & pink veins, mostly carbonate.

Indurated chloritic cataclasite with folation & carbonate veins parallel to principal slip zone (PSZ). Transitions to ultracataclasite nearer PSZ, with lensoid protolith clasts and uniformly silt matrix. PSZ is scaly, foliated ultracataclasite with ~2 mm clay gouge zone. Footwall side of PSZ is foliated, less indurated cataclasite with gouge horizons. Scaly, anastamozing mm-scale internal foliation oblique to PSZ.

Larger phacoidal clasts of dark green, heavily chloritized, fine-grained cataclasite, of host rock protolith; clasts up to 30 cm long.

Occasional 2 cm clasts in dark brownish green to greenish-brown-gray clay matrix. Colors segregated in ~1/2 cm-thick layers. Cataclastic rock, less cohesive than cataclasites nearer to principal slip surface. Veins of epidote, quartz, and carbonate.

Discontinuous body of nearly intact but fractured hornblende-pyroxene quartz diorite. Carbonate veins ~1–8 mm thick spaced ~1–20 cm apart.

Cohesive but heavily jointed chloritic hornblende–biotite monzogranite. Deformed epidote veins. Some heavily jointed areas with clay gouge 2-10 mm wide. Clay gouge contains ~50% monzogranite clasts (fine sand–3 mm diam.).

Fractured hornblende–pyroxene quartz diorite. Less jointed than nearer to PSZ but fractured into ~20 X 50 cm blocks bound on outcrop surface by 3–5 faces. Discontinuous carbonate veins 2–6 mm wide, spaced ~8 cm apart. Some joints 2–10 mm wide and heavily jointed areas with clay zones 2–10 mm wide. Clay zones contain ~50% quartz diorite clasts (fine sand–3 mm diam.).

Chloritic hornblende–biotite monzogranite; more fractured than zone immediately to south. Phacoidal syenogranite clasts ≤10 cm forming sub-vertical fabric. Clay gouge horizons 2–10 mm wide. Gouge contains ~20% syenogranite clasts at ~1 mm diameter.

Highly damaged zone with ≤6 cm phacoidal clasts of hornblende–pyroxene quartz diorite typically bound by clay gouge. Minor ~2 mm carbonate–epidote veins.

Highly jointed zone with both fine-grained hornblende–pyroxene quartz diorite and monzogranite juxtaposed throughout. Phacoidal clasts up to ~15 cm length within damaged matrix. Smaller clasts (~1 cm) form a weak fabric. ~50% silt- to coarse sand-sized quartz and feldspar matrix with a weak fabric oblique to clast fabric.

Pervasively jointed carbonate vein swarm with minor quartz. Bound to S by ~4 mm wide zone of ~20% coarse sand within clay matrix.

Carbonate vein in jointed biotite–hornblende–two-pyroxene monzonite–monzodiorite with 15–20% silt–fine sand damage matrix.

Extensively jointed biotite–hornblende–two-pyroxene monzonite-monzodiorite but with ~1-15 cm coherent blocks in a matrix of only ~20% smaller grains. Joints less extensive than nearer PSZ.

Biotite–hornblende–two-pyroxene monzonite-monzodiorite with minor sulfides. Damaged silt-sand-sized matrix surrounding coherent blocks is only ~10% of total rock area. Coherent clasts up to ~30 cm; avg. 8 cm long. Joints increasingly less extensive toward N.

Dominant biotite–hornblende–two-pyroxene monzonite-monzodiorite becomes still less fractured, with <5% unconsolidated coarse sand particles restricted to only joints between mostly coherent rock. Some large, pink, fairly continuous carbonate veins with white margins.

B

N=31

Fig. 6. (A) Schematic descriptive section of part of the Smithy Creek Fault core, measured oblique to the fault surface at ground level at a roadcut on State Highway 6, South Westland, New Zealand. Location of measured section is indicated in Fig. 7B. (B) Stereoplot of selected planar structural elements represented in fault log. Large black dot is the Smithy Creek Fault plane, green squares are veins, red triangles are foliation measurements, purple diamonds are clay-filled fractures, gray dots are boundaries of representative clasts >1 cm, and red circle is foliation of the ultracataclasite zone in the hanging wall adjacent to the principal slip zone. Filled symbols are from the footwall and hollow symbols are from the hanging wall. (For interpretation of the references to color in this figure legend, the reader is referred to the web version of this article.)
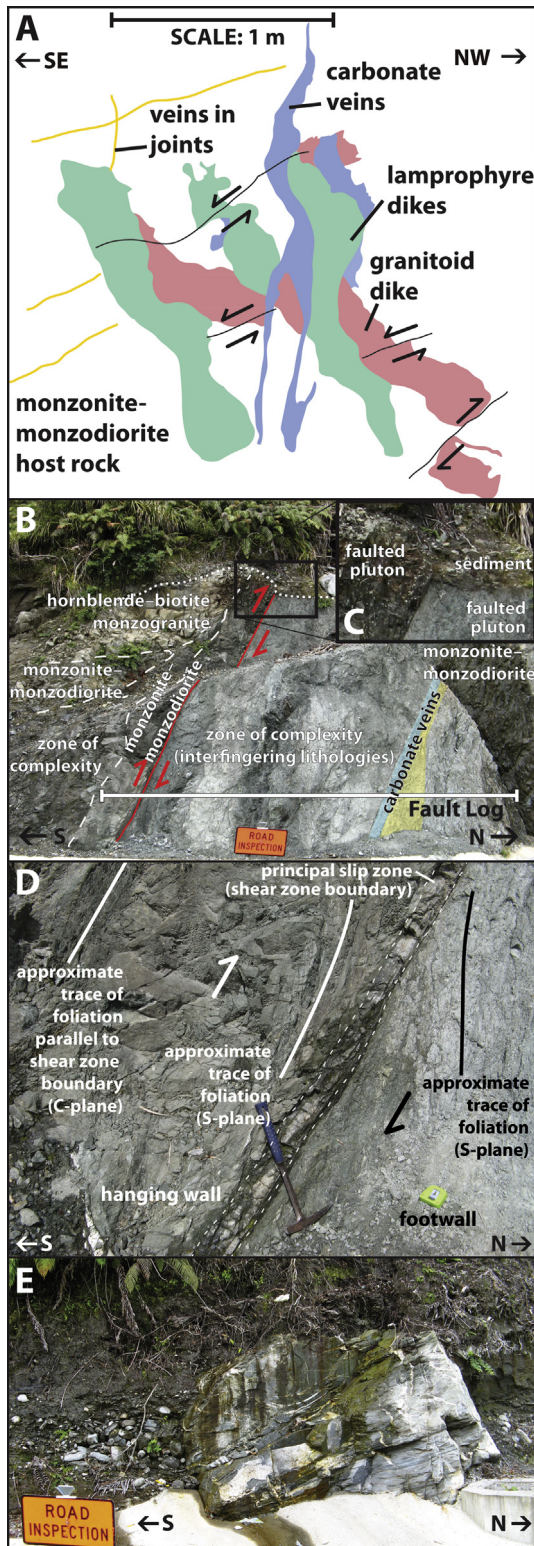
Fig. 7. (A) Simplified schematic diagram of crosscutting relationships in the footwall damage zone, constructed from a tracing of a photograph. Red is an unidentified granitoid intrusion, green represents lamprophyre dikes, blue represents dense networks of calcite veins, and uncolored areas are the biotite–hornblende–two-pyroxene monzonite–monzodiorite host pluton. Yellow lines are joints containing carbonate veins. Black lines are selected small-offset faults. Some faults offset older granitoid dikes but not nearby lamprophyres, while others offset lamprophyre dikes and carbonate veins. The uppermost indicated small fault offsets the lamprophyre to the left (SE) but not the nearby lamprophyre to the right (NW). Image extent is shown in Fig. 3. (B) Photograph of the Smithy Creek Fault core. Dotted white line is the disconformity at

the fault core, and the morphology of the discontinuity between rock and overlying glacial sediments (Section 4.1.3). The footwall fault core comprises a shear zone with parallel boundaries, which allow determination of shear sense based on asymmetric fabric elements. The principal slip surface (to the south, at the footwall–hanging wall interface) is one boundary; two large carbonate veins that form the boundary between the fault core and damage zone in the footwall comprise the other (northern) boundary (Fig. 7B). The hanging wall fault core is also a shear zone bound on the north by the principal slip surface (at the interface with the footwall) and on the south by a subparallel boundary characterized by a gradual change in grain size and degree of induration. Subvertical cataclastic flow fabrics within both zones are oblique to shear zone boundaries and indicate compatible hanging wall-up senses of shear (assuming an S–C-type relationship; e.g. Reinen, 2000; Ikesawa et al., 2003; Van der Pluijm & Marshak, 2004) (Fig. 7D). C-type shear bands in the footwall cataclasite vary in orientation between being subparallel to the principal slip surface (shear zone boundary oriented 090/70 S) and diverging by 19° (071/77 S) (Fig. 7D). Discontinuous hanging wall cataclastic shear bands merge into parallelism with the principal slip surface but in places (e.g. 153/48 SW) include an angle of up to 57° with the shear zone boundary. These relationships indicate top-to-the-northwest sense of shear.

4.1.3. Age of faulting

A disconformity between hard rocks and overlying glacial sediments (Cox & Barrell, 2007) is displaced upward by more than 0.5 m on the hanging wall side, further supporting an oblique-thrust sense interpretation (Fig. 7B–C). Increasing joint density, crumbly appearance, and reddish coloration in hanging wall rocks toward the disconformity with the overlying sediments demonstrate that the plutonic rocks underwent surface weathering prior to deposition of the sediments. Steepening beds nearest the disconformity suggest onlap. Cross-bedding, rounded clasts, and structures such as warped beds resulting from soft-sediment deformation all suggest a glaciofluvial origin, but the large diversity of clast sizes could also indicate deposition as ice contact stratified drift. The existence of laminated silt and sand means that deposition as till is unlikely. A large (~2.5 m diameter), subangular greywacke boulder (Fig. 7E) within the cobble interbeds may also have been deposited glacially (i.e. a "drop stone" or in till) or as ice contact stratified drift. Sediments deposited during the last glacial maximum time reach thicknesses up to 500 m to the west of the Alpine Fault (Norris & Cooper, 1995), but are significantly less thick than this at the study area (≤5 m).

A maximum slip rate can be calculated from the vertical offset at the disconformity, assuming the scarp was glacially eroded during the last glacial maximum at ~65–10 ka (Norris & Cooper, 1995). Estimating the fault slip rate based on offset since 10 ka provides

the base of the overlying glacial sediments (faulted plutonic rocks below line), red line and shear indicators represent principal slip surface, and yellow and blue areas are two major dike swarms near the northern end of the footwall damage zone. Fault Log line is the approximate extent of the measured fault core section (Fig. 6). The extent of this photograph within the outcrop is indicated in Fig. 3. (C) Enlargement of apparent upward deflection of the disconformity with glaciofluvial sediments on the hanging wall side of the principal slip surface, which demonstrates syn- or post-glacial reverse dip-slip motion localized on this surface. (D) Photograph of fault core fabrics indicating a hanging wall-up sense of shear, assuming foliation is perpendicular to maximum principal stress. (E) Photograph of a large greywacke boulder surrounded by poorly sorted gravel and finely laminated mud deposited above a disconformity with underlying plutonic basement. Boulder was likely deposited by glaciers and sediments may have been fluvially deposited. Sign width is 1 m. Photograph taken ~25 m SSE of Smithy Creek Fault principal slip surface (above hanging wall). (For interpretation of the references to color in this figure legend, the reader is referred to the web version of this article.)
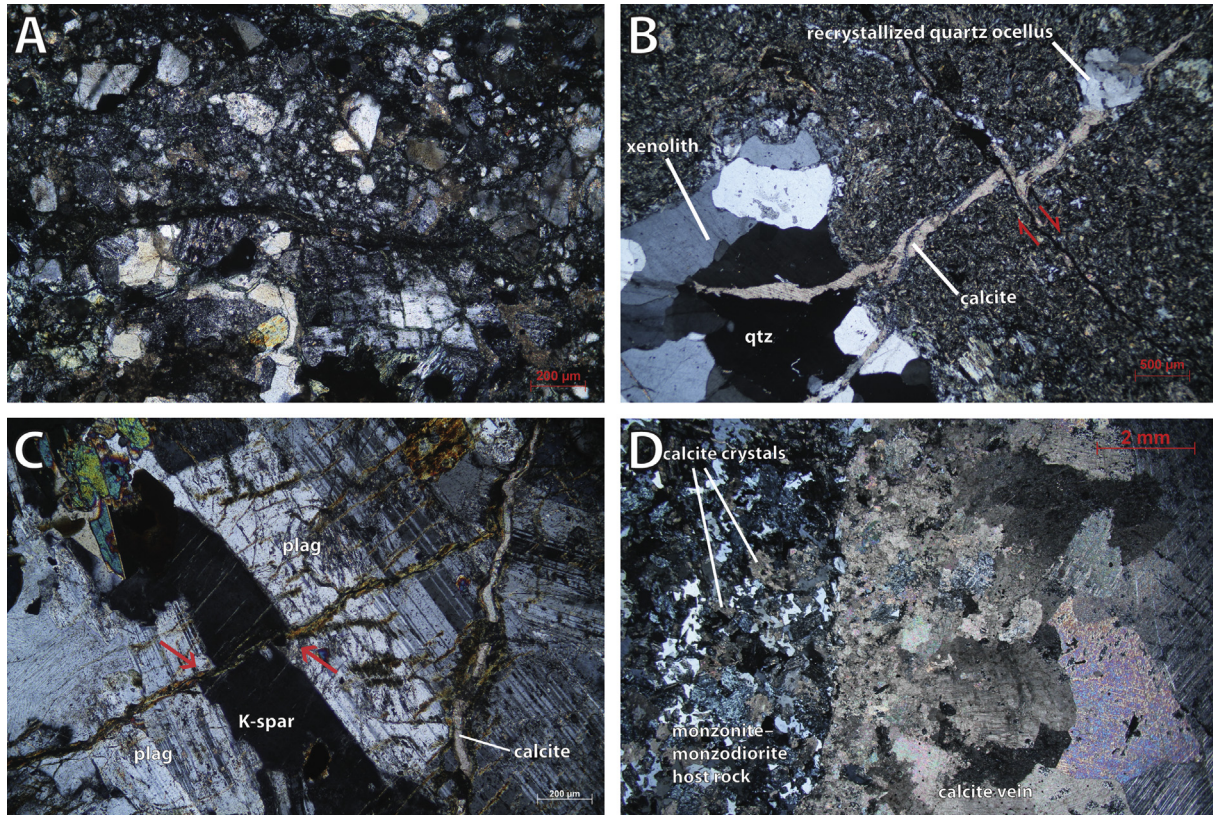
Fig. 8. (A) Photomicrograph of cataclasite fabric from the footwall fault core, XPL. Large angular clasts are mostly feldspar with rarer quartz, hornblende, biotite, and chlorite alteration. (B) Photomicrograph of lamprophyre dike, XPL. Note pink calcite veins intruding quartz ocellus and xenolith but offset by late microfault. Generally, ocelli truncate calcite veins but some veins cut ocelli, where they are thinner than where they cut the host rock. Dark fracture offsets calcite vein (shear arrows). (C) Photomicrograph of veins in biotite–hornblende–two-pyroxene monzonite–monzodiorite, XPL. Narrower muscovite ± epidote vein (arrowed) offsets orthoclase ("K-spar") and plagioclase feldspar grains. Aligned muscovite ± epidote veins are visible within feldspars. (D) Photomicrograph of the margin of a calcite vein with characteristic twinning, XPL. West side of image is wall rock, with many <1 mm calcite crystals throughout. Note fine calcite grains within the vein, adjacent to the vein margin, and increasing grain size toward the center of the vein. (For interpretation of the references to color in this figure legend, the reader is referred to the web version of this article.)

a maximum rate of fault slip, while calculating a slip rate since the beginning of the glacial maximum (~65 ka) provides an intermediate estimate of the slip rate, because it is not known for certain whether glacial or earlier processes eroded the hard rocks. For the slip vector indicated by striae (~31/103), vertical offset of >0.5 m at the disconformity requires >0.53 m dip-slip movement and >0.98 m total oblique slip. Thus we calculate a 9.8×10^{-5} m yr^{-1} maximum slip rate, while the intermediate slip rate (0.98 m over 65 ka) is 1.5×10^{-5} m yr^{-1}.

4.1.4. Discontinuities and veins

The footwall fault core contains abundant chlorite + epidote veins, ranging from 0.5 to 5 cm to meters in length. Many fault core veins have been fractured. They are either subvertical (slightly oblique to the principal slip surface but subparallel to the shear zone fabric) or subparallel to the principal slip surface, but become less aligned further from the principal slip zone. Veins are composed of carbonate ± epidote ± quartz ± feldspar. The fault core (particularly in minty–dark green gouge zones) contains more chlorite + epidote alteration and veining than the host rock and we infer that this assemblage reflects enhanced fluid flow through the fault core compared with the wall rock. Epidote ± quartz ± Mg-carbonate veins are restricted to the fault core and epidote + carbonate veins to within ~12 m of the principal slip zone. Other types occur throughout both the fault core and the surrounding damage zone. Epidote veins commonly also contain a dark gray clay horizon. Larger, massive pink calcite veins generally have cream-colored rims <0.5 cm thick. Calcite

veins (Fig. 8D) commonly form networks (with thicknesses of ~1–5 mm) of many smaller, densely packed, anastomosing veins. Two adjacent carbonate vein networks, each ~10–30 cm wide (6.2–6.6 m on Fig. 6), distributed in an en echelon arrangement within a zone subparallel to the principal slip zone, are not crosscut by other veins. This networking character is prominent also in one large (~1.5 m thick, ~6 m tall) swarm of dense, white carbonate veins <1–8 cm thick (typically 4–5 cm thick) located in the damage zone near Smithy Creek. Veins are found in most rock types except a few of the granitoid dikes (Fig. 8). The distributions of alteration assemblages and vein mineralogies are summarized in Table 2. It is not clear how many episodes of carbonate veining are recorded, but some carbonate veins are zoned, having margins 1–5 mm thick of different color than the vein interior, others are unzoned, and still others are multiply zoned. No clear temporal relationship can be established between these different morphologies. None of the various composition granitoid dikes crosscut one another but lamprophyre dikes (Fig. 8B) cut some granitoid dikes (Fig. 8C). Lamprophyre and most granitoid dikes are also offset along small faults, some of which are mineralized. Carbonate veins occur within some joint planes (Fig. 7A); this is particularly evident in a SE-dipping joint set in the footwall damage zone near Smithy Creek, to the northwest of the principal slip zone.

In thin section, calcite veins are commonly massive and blocky, with some individual crystals ≥1 cm and having 120° grain boundary intersections. Many of the same veins are zoned parallel to vein margins, with the smallest grains on vein walls

Table 2
Distribution of veins and alteration assemblages in the Smithy Creek Fault core and damage zone.

Vein or alteration assemblage	Lithologies affected	Spatial distribution in fault zone	Notes
Carbonate veins	In all except salmon pink monzogranite dike and white biotite syenogranite dike in the damage zone	All of fault zone but most common in fault core. Most voluminous vein mineralogy	Millimeter- to outcrop-scale veins common throughout fault zone, sometimes occurring in networks. Some are zoned. In damage zone, mm–cm offsets across some veins and others offset along fractures. Veins in fault core commonly broken, likely from fault damage. Ca carbonate most common; rare Mg carbonate in fault core
Chlorite veins	Most commonly in dominant pluton	Mostly in fault core but some in damage zone	Millimeter and sub-millimeter scale. Small offsets across some veins
Epidote ± carbonate ± muscovite veins	Mostly in cataclasites, host pluton and millimeter-scale fractures in hornblende syenogranite dike	Mostly in footwall fault core but some in damage zone	Epidote veins often broken in fault core, likely from fault damage. Small offsets observed across some veins outside fault core
Opaque minerals (mostly pyrite)	In fractures and veins in lamprophyres and most granitoid dikes	Throughout but mostly in damage zone	
Quartz and feldspar in veins	In salmon pink monzogranite dike	In damage zone	Appear to be partially healed joints and microfaults
Sericite alteration of feldspars	All	Pervasive throughout	
Alteration of amphiboles, feldspars, and phyllosilicates to chlorite	All but especially in chloritic hornblende–biotite monzogranite in fault core	Contributes to minty green coloration throughout fault zone but especially in fault core	
Disseminated calcite crystals	In all except salmon pink monzogranite dike and white biotite syenogranite dike in the damage zone	Throughout but more common in fault core	
Petrologic character and assemblage indicating overall hydrothermal alteration	All but especially in voluminous porphyritic hornblende–pyroxene quartz diorite having mineral replacement characteristics indicative of greenschist metamorphism	Throughout but most significant in fault core	

suggesting that crack-seal processes were important as they formed (Van der Pluijm & Marshak, 2004; Fig. 8D). Rare fractures cut calcite crystals and many of these fractures also contain calcite. Calcite crystals are disseminated in the wall rock but decrease in abundance away from the vein. Smaller, anastomosing veinlets (~0.5–2 mm) with irregular margins and angular crystals of varying size branch off of the main vein into the host rock, and 100–200 μm thick veinlets with sharp margins also branch off larger veins.

Within the damage zone small faults with minor (1–30 cm) offset are common, and brittle microfaults with small (<1 mm) offsets are observed in thin section in all lithologies, including the host pluton. Because brittle structures or characteristic vein mineralogies are sometimes observed to be absent in a lithology that, based on crosscutting relations, is younger than a neighboring lithology containing the same type of structure, the presence or absence of microfractures is not a good relative age marker in these rocks (Passchier, 2008). In some cases, small faults offsetting one lamprophyre or granitoid intrusion do not offset another nearby intrusion of the same composition (Fig. 8B). This likely indicates that fracturing differentially affected the heterogenous rock mass. Vein emplacement and hydrothermal alteration also appears heterogenous, with some plutonic lithologies or locations in the fault zone affected by different vein mineralogies or alteration assemblages (Table 2). The zoned character of some carbonate veins indicates that some vein emplacement was polystage. Two prominent, subvertical faults crosscut all other joints within the Smithy Creek Fault damage zone (Fig. 3) and are thought to be among the youngest structures in the study area because (1) they are not offset along any small faults, and (2) they

have not been affected by the mineralization that pervades the main fault core and damage zone.

4.2. Orientation data

Two prominent clusters of compass-measured vein orientations have means at 064/77 SE and 074/82 SE (Fig. 9A). Granitoid dikes have mean orientations of 006/74 E and 092/82 S from photogrammetry and three dike orientations were measured in the field (Fig. 9B). However, many veins and dikes are anastomosing and not consistently planar; orientation data collected both by hand and from photogrammetry reflect only planar to subplanar features.

Compass-measured discontinuities (some with slickensides) also display clustered orientations. Mineralized slickenfibres consistently cluster about 38/083 and 43/112 (Fig. 10A) on an average shallowly SE-dipping fracture plane. Slickenlines, which are lineations distinguished by the absence of mineralization on the surface, cluster strongly at ~28/078 (Fig. 10B) on an average moderately SE-dipping fracture plane. The bimodal clustering in both datasets suggests that there were two major slip directions. Some joints measured in the field contain a clay horizon but no slickensides. These planes have a mean orientation of 108/72 S. The total combined average orientation of all compass-measured fracture planes, including a small group of joints lacking both slickensides and clay horizons, is 040/47 SE (with a minor cluster at 103/41 S), which is very similar to the average of uncorrected planes from photogrammetry (042/60 SE); this suggests that the Terzaghi (1965) correction may be unnecessary (Fig. 11A–C). All compass-measured fractures lacking a clay horizon have a
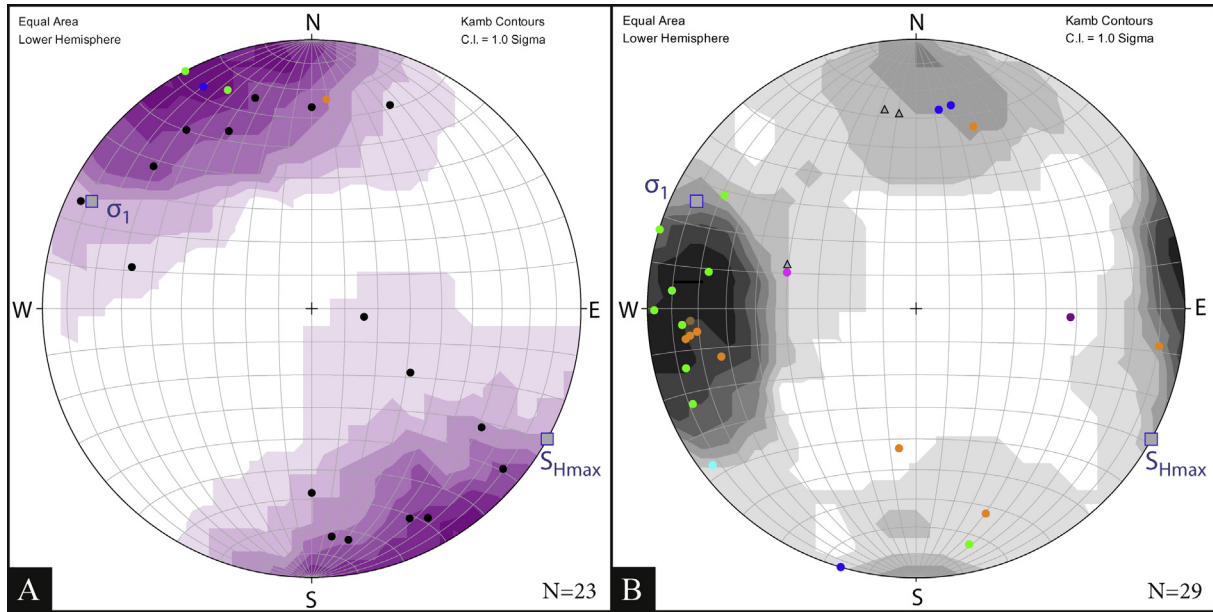
Fig. 9. Stereoplots of poles to planar components in the Smithy Creek Fault zone, with Kamb (1959) contouring of clusters of poles. Blue squares with gray centers represent the local maximum principal stress (σ_1) and maximum principal horizontal stress (S_{Hmax}) azimuths calculated from seismic inversion (Townend et al., 2012). (A) Compass-measured planar vein orientations with Kamb contouring of clusters of poles. Black dots are carbonate veins, orange dots are veins containing both clay and carbonate, blue dots are veins containing quartz and/or feldspar, and green dots are epidote veins. (B) Granitoid dike orientations from compass measurements (black hollow triangles) and dikes and large veins from photogrammetry (round dots colored by photo number). (For interpretation of the references to color in this figure legend, the reader is referred to the web version of this article.)

significantly different mean orientation (120/69 SW) to the mean orientation of all fractures without a clay horizon (033/49 SE; Fig. 9A). Terzaghi (1965)-corrected clusters of discontinuity planes from photogrammetry are oriented 042/70 SE, 145/73 NE, and 007/54 E (Fig. 11B). The two immature faults are subvertical and strike ~075, which is significantly different from these other types of faults and veins.

5. Kinematic inversion of discontinuity data

5.1. Fault-fracture mesh comparison

According to classic Andersonian theory (Anderson, 1951), groups of related structures called "fault-fracture meshes" are expected to form in intact, isotropic rock at shallow crustal levels in

Fig. 10. Stereoplots of lineated joints, measured by compass, with Kamb (1959) contouring of lineations. Blue squares with gray centers represent the local maximum principal stress (σ_1) and maximum principal horizontal stress (S_{Hmax}) azimuths calculated from seismic inversion (Townend et al., 2012). (A) Joint planes (great circles) having mineralized slickenfibers (lines). (B) Joint planes (great circles) having unmineralized slickenlines (lines). (For interpretation of the references to color in this figure legend, the reader is referred to the web version of this article.)
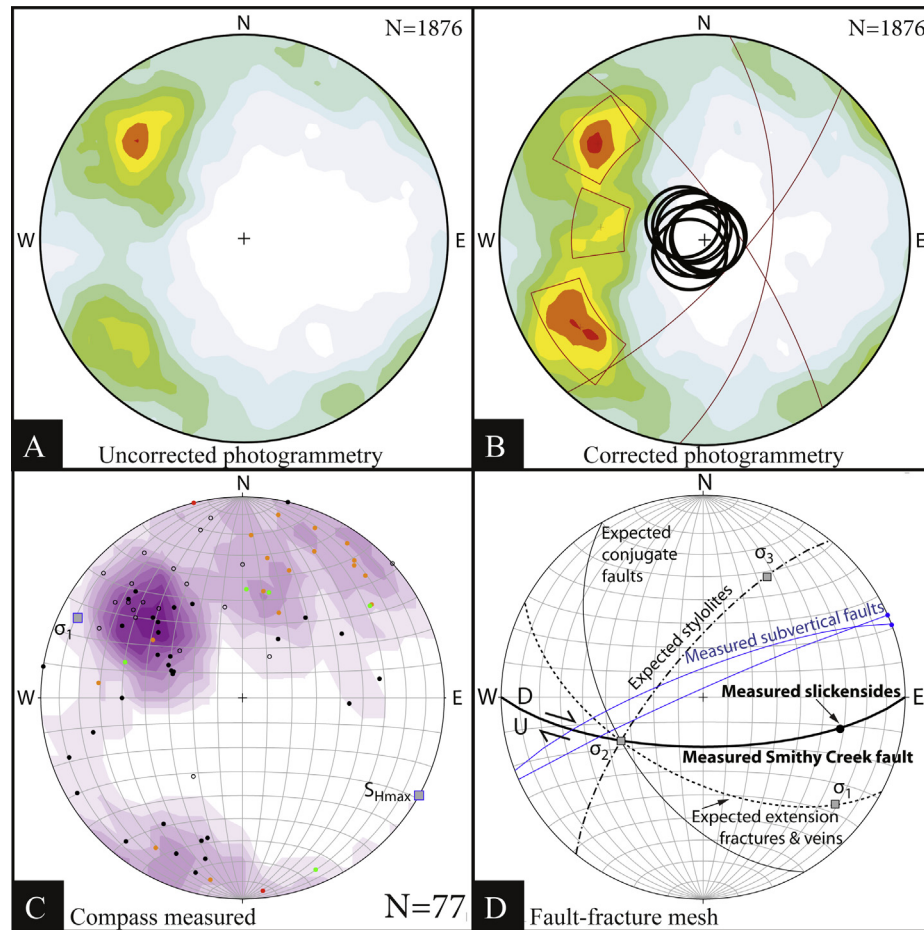
Fig. 11. (A) Stereoplot of poles to uncorrected discontinuity data measured from photogrammetry, combined from all photopairs. Clusters are at 044/71 NE and 140/74 SE by Fisher et al. (1987) contouring. (B) Discontinuities from all stereophotos measured from photogrammetry and corrected for orientation bias by the Terzaghi (1965) method, with Fisher et al. (1987) contouring. Clusters of planes are at 042/70 SE, 145/73 NE, and 007/54 E, by Fisher et al. (1987) contouring. (C) Compass-measured fracture data with Kamb (1959) contouring. Blue squares with gray centers are local maximum principal stress (σ_1) and maximum principal horizontal stress (S_{Hmax}) azimuths calculated from seismic inversion (Townend et al., 2012). Note that the clustering matches best with the uncorrected data in (A), suggesting that Terzaghi (1965) correction may be unnecessary. (D) Stereoplot showing structural components of an inferred fault-fracture mesh associated with the most recent slip vector of the Smithy Creek Fault, including predicted orientations of stylolites (dot-dash great circle), extension fractures and veins (dashed great circle), conjugate fault orientations (solid thin great circle), and principal stresses. Orientations of two immature strike-slip faults in the footwall damage zone, calculated from photogrammetry, are shown in blue, with horizontal slip vectors assumed due to the steep dips of these faults. (For interpretation of the references to color in this figure legend, the reader is referred to the web version of this article.)

response to high differential stress ($\sigma_1 - \sigma_3$), or negative effective normal stress (σ_3') when fluid pressure ($P_f > \sigma_3$ (Hill, 1977; Sibson & Scott, 1998; Sibson, 2000). Tension cracks (joints) are expected to form in the plane containing σ_1 and σ_2, and two conjugate fault orientations, symmetrically oriented perpendicular to σ_1 and σ_3, and containing σ_2, are possible (Secor, 1965; Hill, 1977; Sibson, 2000; Oliver & Bons, 2001; Van der Pluijm & Marshak, 2004). Deviations from the Anderson (1951) model may arise if faulting involves reactivation of an older fault surface (e.g. Bruhn et al., 1982; Sibson, 1985; Scholz, 1998), the host rock is anisotropic (e.g. Peacock & Sanderson, 1992), or there is a variable stress field caused by fluid pressure and changes to the elastic properties of rock in the damage zone by fracturing (Faulkner et al., 2006), or at coarse scale by topographic relief for fault zones near the surface (Norris & Cooper, 1997). If P_f is high, local rotation of the stress field can also cause slip to occur on fault planes oriented unfavorably with respect to the principal stress axes without inducing extensional fracturing (Faulkner et al., 2006).

Nevertheless, based on this theory and the assumption that fracturing occurred in isotropic rock with no weak, pre-existing faults or fractures, we have predicted orientations of the three principal stresses from the orientation of the main Smithy Creek

Fault, as follows: The principal slip surface is oriented 090/70 S, with minor local variation. Slickensides on the slip surface are oriented $\sim 31/103$, which is the orientation of the slip vector (Fig. 11D). Based on these inputs, and employing relationships predicted by classical Mohr–Coulomb theory, σ_2 is expected to be 52/242. The reverse right-lateral dip-slip sense determined from outcrop characteristics requires that the fault surface be the more northwesterly-dipping of the two possible conjugate faults predicted. Therefore, σ_1 is 17/129 and σ_3 is 33/028. These principal stress orientations (Table 3) are similar to the modern stress state obtained from seismic inversion (Leitner et al., 2001; Townend et al., 2012), suggesting that the most recent slip occurred in the current tectonic regime. We then predict the orientations of the remainder of the fault-fracture mesh from these stress orientations (Fig. 11D).

These expected structure orientations are not compatible with joint and vein orientations measured from photogrammetry and by field compass (Figs. 9A, 10, and 11A–C), which suggests the Smithy Creek Fault is oriented unfavorably relative to the stress state that produced the exposed fracture and vein networks. For this reason, we conclude that this fault is a reactivated structure, rather than one that formed in the modern stress regime. The orientations of the small, subvertical faults at the study area

Table 3
Orientations of the maximum principal stress (σ_1; equivalent to maximum elastic strain axis) determined from various methods here and from previous publications.

Orientation of maximum principal stress (σ_1; equivalent to maximum elastic strain axis)	Method	Location	Source
17/129	Fault-fracture mesh analysis of a fault plane oriented 090/70 S with slip vector 31/103 (main fault)	Study area	This study
00/101	Fault-fracture mesh analysis of a fault plane oriented 074/86 with slip vector 00/074 (minor faults)	Study area	This study
~24/133	Aleksandrowski (1985) method of fractures with slickenfibers	Study area	This study
~10/296 (~00/119 for horizontal S_{Hmax})	Seismic inversion	Near Herepo, South Island	Townend et al. (2012)
30/119	Seismic inversion	North of Mount Cook, South Island	Leitner et al. (2001)

(~074/86 N) can also provide information about the local stress field during slip. If a horizontal slip vector is assumed on these faults (reasonable given their subvertical orientation), fault-fracture mesh analysis predicts σ_1 orientations of either 00/046 or 00/101, dissimilar to the modern stress state obtained from seismic inversion. Because we have demonstrated likely reactivation of the main oblique thrust, and this method does not adequately consider existing anisotropy, we conclude that the fault-fracture mesh method is inadequate for independently calculating principal stress orientations. We instead compare these stress orientations with the results of a methodology devised by Aleksandrowski (1985) to estimate these stress orientations from slickensided fracture surfaces in anisotropic rock.

5.2. Aleksandrowski (1985) method

Arthaud (1969), and many subsequent workers, including Aleksandrowski (1985) and Twiss and Gefell (1990), proposed that orientations of lineations on joint surfaces, particularly mineralized

slickenfibres, can be analyzed to independently deduce the principal stress directions and shear sense of a brittle fault zone, provided that they formed coevally. These 'stress inversions' assume that principal stress orientations parallel principal strain axes; a reasonable assumption for small elastic strains and subsequent brittle failure. However, we think it is most realistic to acknowledge this assumption explicitly and thus refer to the axes thus obtained as those defining the elastic strain ellipsoid. The Aleksandrowski method (Section 3.3; Appendix B) is especially useful if the fault plane orientation deviates from that predicted for a particular stress regime by Mohr–Coulomb theory, as is the case here. This method also does not require sense-of-shear indicators or slickenfibers, but an underpinning assumption is that all analyzed slickensides resulted from movement during a single tectonic episode. Unmineralized and mineralized fractures with slickensides were considered separately, since shearing on joint surfaces from different episodes might be associated with different mineralizing conditions.

Intersection points, which could be principal elastic strain axes (S_1, S_2, or S_3), are shown in Fig. 12A–C. Data are very limited for unmineralized slickenlines (Fig. 12B). The combined dataset produced clusters of intersections 86 ± 1° apart (Fig. 12C) but clusters of intersections for mineralized slickenfibers are only 63° apart (Fig. 12A). However, if S_2 and S_3 were of similar magnitude and significantly smaller than S_1, varying S_2 and S_3 orientations around a girdle/great circle broadly perpendicular to S_1 might be expected. This relationship is observed in Alpine Fault hanging wall structures in the adjacent Waiho Valley (Fig. 1), which include both subhorizontal and subvertical extension fractures that reflect nearly equal magnitudes of S_2 and S_3 (Norris & Cooper, 1986). The principal strain axis orientations obtained from only mineralized slickenfibers are expected to be the least likely to record slip from multiple different tectonic episodes, and hence to be the most robust means of determining a maximum principal stress orientation. The ~24/133 cluster from this dataset is interpreted to reflect the orientation of S_1, based on the top-to-the-northwest sense of shear observed in the Smithy Creek Fault (Table 3).

6. Discussion

Detailed characterizations of the Smithy Creek Fault core and damage zone, including vein mineralogy, together with fracture and slickenside orientation analyses based on 3-D digital
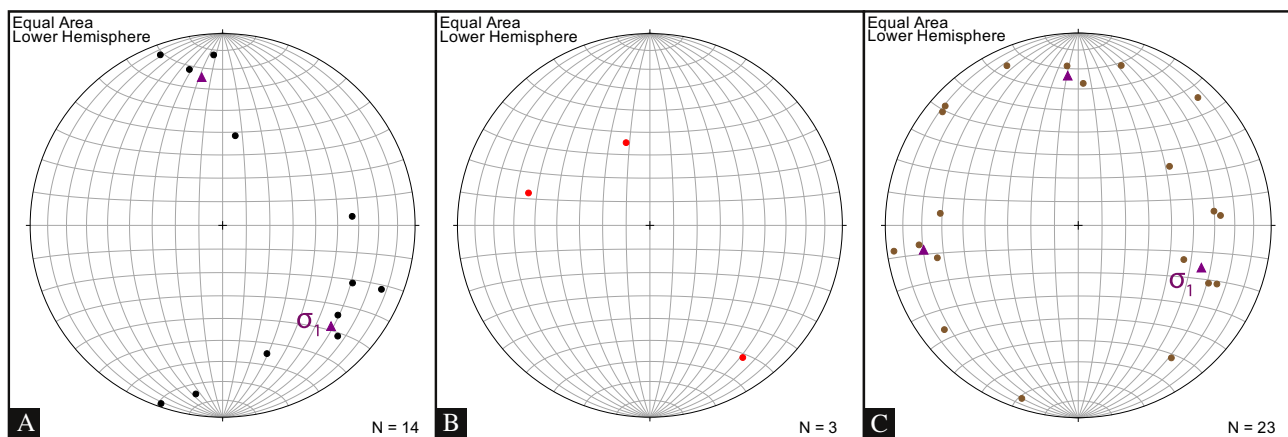

Fig. 12. (A)–(C) Results of Aleksandrowski (1985) method. Figures are stereoplots of intersection lineations between great circles connecting slickensides (GCFs) and great circles connecting poles to M-planes (GCPs) for one common intersection point (CIP) of M-planes. Dots are GCFs with more statistically significant best-fit great circles. CIPs and M-planes are shown in Appendix B. Purple triangles are estimated centers of lineation clusters. (A) Mineralized slickenfibers. (B) Unmineralized slickenlines. (C) Intersection lineations between GCFs and GCPs from CIPs between combined slickenfiber and slickenline datasets. (For interpretation of the references to color in this figure legend, the reader is referred to the web version of this article.)

stereophotos and field measurements, enable reconstruction of its history of movement and allow inferences of permeability evolution.

6.1. Development of less mature, subvertical faults

The two immature (Section 3.4), subvertical, gouge-filled faults exposed near the Smithy Creek Fault are subparallel to nearby Alpine Fault-related traces interpreted from LiDAR to strike ~090–140° (Barth et al., 2012; Fig. 1), which suggests that the features may be immature strike-slip structures related to the Alpine Fault. Two compass measurements from different parts of one of these structures were 074/86 NW and 076/90, and average overall orientations obtained from photogrammetry were 066/86 NW and 068/79 NW for each of the two structures. In addition, the average discontinuity orientation at Smithy Creek, of 040/47 SE, is similar to the average orientation of major reverse segments of the Alpine Fault at depth (040–045/50 SE), further suggesting partitioning of Alpine Fault-related damage into the Pacific Plate footwall (Barth et al., 2012). Another Alpine Fault trace identified by Barth et al. (2012) strikes ~140° and extends NW out of the coverage area in the direction of the Smithy Creek Fault (Fig. 1). These observations support the hypothesis that the Smithy Creek Fault and its younger crosscutting structures comprise a rare exposure of part of a "third-order" Alpine Fault flower structure incorporating Western Province rocks of the Australian Plate footwall.

A maximum principal stress (σ_1) orientation of ~10/296 (Table 3) and a maximum principal horizontal stress (S_{Hmax}) of ~119° were obtained for the vicinity of Herepo (Fig. 1), near the study area, from inversion of earthquake focal mechanisms (Townend et al., 2012). This orientation is similar to the ~24/133 cluster of S_1 we infer by Aleksandrowski's (1985) slip inversion method (Table 3). Because a large spread of intersection lineations were obtained using the Aleksandrowski (1985) method, the results probably have large errors, so the principal elastic strain axis orientations derived by this method are likely statistically similar to stress axis orientations inferred from earthquake inversion. The most recent movement on structures in the study area therefore appear to be controlled by the same stresses that control the Alpine Fault and hence that some plate boundary strain must be partitioned onto the Australian Plate, at least very near the Alpine Fault.

Fault-fracture mesh analysis yielded possible σ_1 orientations of either 00/046 or 00/101 based on the orientations of these structures, assuming a horizontal slip vector (Section 5.1). The first value is plainly not in accordance with the orientation presently recognized from earthquake focal mechanisms around the Alpine Fault, nor with local principal elastic strain (S_1) orientations obtained here from the Aleksandrowski (1985) method, but the 00/101 orientation is not significantly different from the Townend et al. (2012) and Leitner et al. (2001) results. It is unclear whether either the subvertical small faults or the larger oblique thrust remain active, or both, although the larger oblique thrust is a significantly more mature structure with a large fault core and damage zone, indicating that movement on that structure likely began significantly earlier than on the younger, unmineralized subvertical structures. If faults of both geometries have been active simultaneously, this arrangement resembles the partitioned geometry of the Alpine Fault, with separate predominantly oblique thrust and dextral strike-slip segments, but the larger oblique Smithy Creek Fault is also predominantly strike-slip. It is possible also that the smaller, subvertical features are Riedel shears associated with the larger Smithy Creek Fault.

Instead of strain partitioning, the difference in orientation between two immature strike-slip faults and the larger Smithy

Creek Fault could arise from these structures having formed at different times. Strong contrasts in the maturity of these smaller subvertical structures compared with the larger Smithy Creek Fault, including little to no mineralization, narrow single gouge zones, and an absence of cataclasite, supports much later development of the subvertical faults. The existence of a subvertical carbonate vein swarm inferred to have resulted from hydrofracturing a few meters from the smaller faults (Section 6.4) is evidence that the Smithy Creek Fault zone experienced significant mineralization and high fluid pressures prior to the onset of the smaller faults, which could have facilitated slip on the larger inherited structure. A drop in fluid pressure could also have facilitated formation of the new structures by removing the fluid pressure mechanism for activation of the unfavorably oriented, inherited Smithy Creek Fault.

6.2. Asymmetry of damage zone

The Smithy Creek Fault is asymmetrical, with ~10–20% of the total >8 m fault core occurring within the hanging wall (the hanging wall damage zone is not fully exposed but the footwall damage zone is >100 m wide). Differences in seismic velocity between contrasting lithologies on opposite sides of the principal slip surface are known to produce asymmetrical damage zones in strike-slip faults, as damage occurs preferentially in faster seismic velocity (the tensional quadrant of the "stiffer" material; Ben-Zion & Shi, 2005; Dor et al., 2006; Mitchell et al., 2011), whereas faulting in homogenous rock is expected to produce symmetrical damage on either side of the fault resulting from symmetrical off-fault plastic strain. Rupture preferentially occurs in the direction of movement of the fault block having slower velocity, which, over multiple slip events, causes disproportionate damage on the high-velocity side (Dor et al., 2008). In addition to material differences, damage asymmetry during inelastic deformation is influenced by the angle (Ψ) between σ_1 and the fault plane; damage will be concentrated in extensional areas if $\Psi \geq 45°$, in compressional areas if $\Psi \leq 15°$, and in both if $15° < \Psi < 45°$ (Templeton & Rice, 2006, 2008).

However, material contrasts are not significant across the principal slip zone of the Smithy Creek Fault, so we cannot draw on the above mechanisms to explain this case. Instead, asymmetry is likely explained by the unique hanging wall P-T-t evolution caused by reverse faulting. The thrust component of slip recorded in the oblique sense slip vector brought hanging wall rocks deformed at greater confining pressures into contact with footwall rocks only deformed at comparatively shallow level. Numerical modeling of strike-slip faults reveals that they typically display "flower structure" geometry at shallow depths after <0.1 km of total fault slip, so they have a broad damage zone at shallow levels but a narrower damage zone at depth (Finzi et al., 2009). Exhumation in this case therefore may have juxtaposed a narrow hanging wall damage zone uplifted from depth and an extensively deformed footwall damage zone developed in the near surface.

6.3. Hydrothermal alteration

Widespread hydrothermal alteration within both the fault core and damage zone indicates significant volumes of fluid flow through them. All lithologies except granitoid dikes have green coloration due to the presence of epidote and/or chlorite (Table 2). Chlorite and epidote veining are especially widespread in the fault core and lesser amounts of chlorite are present throughout the damage zone, including at the furthest exposure from the fault core. The intensity of green coloration

increases into the fault core and helps distinguish its boundary with the damage zone. Mitchell et al. (2011) described a similar change in color and comparable distribution of vein mineralogies, associated with the development of alteration assemblages, at the Caleta Coloso fault in northern Chile, suggesting that both fault cores might have, at one time, been more permeable than their damage zones.

6.4. Structures related to fluids

In addition to reducing the shear stress required to reach the Mohr—Coulomb failure envelope, increasing P_f also makes tensile failure more likely if differential stresses are low (Secor, 1965; Sibson, 1977; De Ronde et al., 2001; Faulkner et al., 2006). Tensile fracture can be promoted by fluid pressure build-up below a layer with low permeability (e.g. Sibson, 2003). The 1—1.5 m wide sub-vertical vein swarm exposed in the Smithy Creek Fault footwall, which consists of many smaller veins with moderate apparent dips to the west, is inferred to have formed by this mechanism. The vertical orientation of the overall group of veins and the networked distribution of smaller veins suggests that many small extension fractures oriented in the $\sigma_1-\sigma_2$ plane may have opened and connected in a complex manner within this channel as a result of overpressured fluid from depth escaping toward lower pressure conditions nearer the surface (Ridley, 1993; De Ronde et al., 2001). The origin of the vertical vein swarm in the Smithy Creek Fault damage zone is incompatible with reactivation of a cohesionless fault because there is no evidence that fluids exploited a single fault surface; rather, the chaotic network of veins indicates rapid extension fracturing.

High-angle reverse faults, such as the Smithy Creek Fault, are oriented unfavorably for slip according to the Anderson (1951) model due to their high angle from typically subhorizontal orientations of σ_1 in compressional settings, so high fluid pressures are often required to reactivate these structures instead of developing new faults with a more favorable orientation with respect to σ_1 (Sibson et al., 1988; Sibson, 1990). P_f was locally high enough to prompt hydraulic fracturing and probably also stimulated reactivation, but would have varied, perhaps in a cyclical manner as described by Sibson (1990, 1992). Periods of low fluid pressure may have facilitated formation of new, unmineralized structures, oriented favorably relative to the prevailing stress state. The two subvertical faults are oriented ~40—55° away from the modern maximum principal horizontal stress calculated by Townend et al. (2012). Significant mineralization in the fault core is inferred to have hydrothermally cemented the fault between seismic events, which increases the cohesive strength of a fault surface, making it more difficult to rupture (Sibson, 1990, 1992). Laboratory studies have found that hydrothermal reactions at elevated temperatures cause gouge compaction and healing of fractures, which can significantly strengthen fractured rock (Tenthorey et al., 2003). For example, experiments on granite at 300—500 °C have found that dissolution, transport, and precipitation of ions by hydrothermal fluid flow can also reduce permeability by orders of magnitude over ~1 year (Moore et al., 1994). This situation may prevent reactivation of the existing structures and hence a failure to relieve fluid pressure, which can result in hydrofracturing (Sibson, 1992; Tenthorey et al., 2003). Strengthening of fault core rocks by hydrothermal cementation probably caused the fault zone to be widened in subsequent slip events as deformation occurred in weaker surrounding rocks (Tenthorey et al., 2003; Wibberley et al., 2008; Caine et al., 2010). At the Smithy Creek Fault, a wide (>8 m), distributed fault core and presence of structures suggesting hydrofracturing supports the idea of a strong, impermeable fault core below which fluid pressures could reach near-lithostatic levels.

7. Conclusions and implications for large fault zones

The Smithy Creek Fault represents a rare exposure in the Western Province footwall of the Alpine Fault zone of a mature, oblique-slip thrust fault that appears to have experienced kilometer-scale displacement due to Australian—Pacific Plate convergence. Pervasive quartz—carbonate—chlorite—epidote mineralization in veins formed in a kinematic regime consistent with modern stresses and proximity to the third-order subsidiary fault segments that comprise the Alpine Fault flower structure suggest close association between modern fluids circulating in the Alpine Fault footwall and fluids responsible for mineral precipitation during evolution of the Smithy Creek Fault. Because granitoids of similar compositions make up the rocks in the hanging wall and footwall of both known exposures, the asymmetric damage zone and fault core are likely not associated with significant compositional contrasts across the principal slip surface as described in many other locations (e.g. Ben-Zion & Shi, 2005; Dor et al., 2006, 2008; Mitchell et al., 2011). Damage zone asymmetry at the Smithy Creek Fault instead appears to be a consequence of the small component of reverse slip in the most recently recorded slip vector, which presently juxtaposes hanging wall rocks deformed at higher temperatures and confining pressures against footwall rocks deformed at shallower levels.

Damage zone and fault core permeability evolved with time, in a manner consistent with the history of hydrothermal sealing related to mineralization, fault zone strengthening, and subsequent overpressure resulting in hydrofracturing described by Caine et al. (2010). With strengthening, subsequent slip widened the fault core and damage zone, resulting in the wide, mature structure exposed presently. The fault core has experienced extensive chlorite and epidote mineralization and displays the characteristic green coloration described by Faulkner et al. (2008) at the Caleta Coloso fault in Chile. Quartz and carbonate veining are also widespread, and a chaotic, subvertical carbonate vein swarm in the footwall damage zone suggests hydrofracturing and subsequent mineral precipitation resulting from fluid overpressure. This structure must precede two similarly-oriented immature (≤20 cm damage zone) gouge-filled strike-slip faults located in the footwall damage zone, within meters of the vein swarm, but which are not significantly mineralized. The mature oblique-thrust fault is oriented unfavorably for reverse slip in the present stress field due to its steep dip, although fault-fracture mesh analysis suggests that its most recent slip nevertheless records some movement related to this stress field. Expected orientations of fault-fracture mesh structures related to the fault plane and recent slip vector are also incompatible with the network of fractures and veins currently exposed in the damage zone, as well as the two younger subvertical faults. Kinematic inversion using methodology developed by Aleksandrowski (1985) of mineralized damage zone structures shows that the fractures developed in an elastic strain field comparable with local modern stress orientations obtained from seismic inversion (Leitner et al., 2001; Townend et al., 2012). The similarity between these published maximum principal stress orientations and the stress/elastic strain axis orientations calculated here (from analysis of the Smithy Creek Fault slip vector and from independent evaluation of slickenfibers on damage zone fractures) indicates that all of these structures experienced brittle deformation in a stress state comparable with the current stress field. With subsequent strengthening of the unfavorably oriented Smithy Creek Fault core, deformation was distributed into the damage zone, where mineralized fractures developed, and where the younger strike-slip faults formed and became preferable for slip.

Appendix A. Orientation bias and ability of photogrammetry to detect a representative set of structures

Several types of orientation bias are known, some of which are functions only of inherent characteristics of the study area such as joint orientation, outcrop orientation, joint spacing, and outcrop relief. Trace exposure bias (Terzaghi, 1965) is introduced by the angle of the outcrop face relative to discontinuity sets (Lato et al., 2010). Discontinuity data collected using digital methods can also suffer biases related to the observer or sampling device, including "line-of-sight bias" (caused by the angle of the scanner (i.e. camera) relative to discontinuity surface orientations), "joint distance bias" (affected by the normal distance of the scanner from various joint surfaces), and "field-of-view bias" (caused by occlusion of parts of the outcrop surface that occur in a particular field-of-view) (Lato et al., 2010). Of these, we expect only "field-of-view bias" caused by occlusion to significantly affect outcrop-window photogrammetric data (as opposed to scan-line data) because the use of two cameras in photogrammetry significantly reduces line-of-sight problems resulting from a single scanner (Lato et al., 2010). Other sources of orientation bias are discussed by Sturzenegger & Stead (2009), but these are difficult to correct. If orientation bias does occur, pooled data should show less bias due to the variable strike of the outcrop face. Nonetheless, the nature of outcrop face orientation we observed would skew interpretations of joint orientations with distance from the principal slip zone because certain outcrop face orientations are better represented than others. In the case of hand compass-measured discontinuities, the investigator's ability to employ many distances, lines-of-sight, and fields-of-view relative to discontinuities while collecting data, combined with the many orientations of outcrop surfaces investigated, suggests these biases will not be significant. Trace exposure bias is the only type of bias considered for hand-collected discontinuity data, as the other types presented here are associated with static viewing locations (Lato et al., 2010).

Minimal occluded areas were observed in the photopairs, so field-of-view bias (Sturzenegger & Stead, 2009; Lato et al., 2010) can be ruled out as a major source of bias. The use of dual camera positions for each photopair reduces occlusion horizontally, although it usually does not affect occlusion vertically unless one camera is placed at a significantly higher elevation or is in some other way able to view surfaces hidden above or below others. The effects of joint distance bias (Lato et al., 2010) should be small compared with other close-range terrestrial remote sensing methods due to the dual camera positions used in 3-D photogrammetry because joint distance bias increases (in favor of detection) as the normal distance between the sensor and a discontinuity decreases (Lato et al., 2010). Line-of-sight bias (Lato et al., 2010) is produced by the angle between the scanner's line-of-sight and the discontinuity surface; discontinuities with surfaces perpendicular to the scanner line-of-sight will be most commonly displayed, whereas discontinuity surfaces parallel to the line-of-sight will be least commonly displayed. However, because line-of-sight error is thought to apply only to single-station static or scan-line LiDAR remote sensing rather than outcrop-window mapping, and because bias observed in the present data appears correlated with outcrop orientation itself, this error is not expected to contribute to bias in this study. Instead, we apply the Terzaghi (1965) correction using Dips software (Rocscience, 2006) to attempt to remove the observed bias in favor of detection of joint surfaces perpendicular to the outcrop face. Terzaghi's (1965) correction applies the weighting factor N to contouring of a set of planar discontinuities, where

$$N = 1/\sin\theta \qquad (1)$$

where θ is the angle between the discontinuity surface normal and the outcrop face normal (Terzaghi, 1965; Lato et al., 2010). A threshold of $\theta \geq 15°$ was applied to prevent zeroing of clusters of discontinuities with orientations parallel to the outcrop face. The corrected data by stereophoto number are shown in Fig. 5. Original, uncontoured data are shown in Fig. A1. Despite minimal observed occlusion, expected "shadow zones" of areas most biased against detection due to this phenomenon are displayed together with the Terzaghi (1965)-weighted data. Occluded planes are expected to be those with a dip and dip direction similar to that of the camera line-of-sight (Sturzenegger & Stead, 2009; Lato et al., 2010; Brideau et al., 2012), and the occurrence of few joint plane orientations in these "shadow zones" may indicate some occlusion. Because of spacing between the camera positions and variable outcrop heights, camera line-of-sight is a rough estimate of the average azimuth and inclination of both photo locations. Both the corrected (Fig. 11B) and uncorrected (Fig. 11A) contoured data accord well with uncorrected hand compass-measured discontinuity data (Fig. 11C), suggesting that the Terzaghi (1965) correction may be unnecessary (Section 4.2), but the corrected data are shown for comparison purposes.
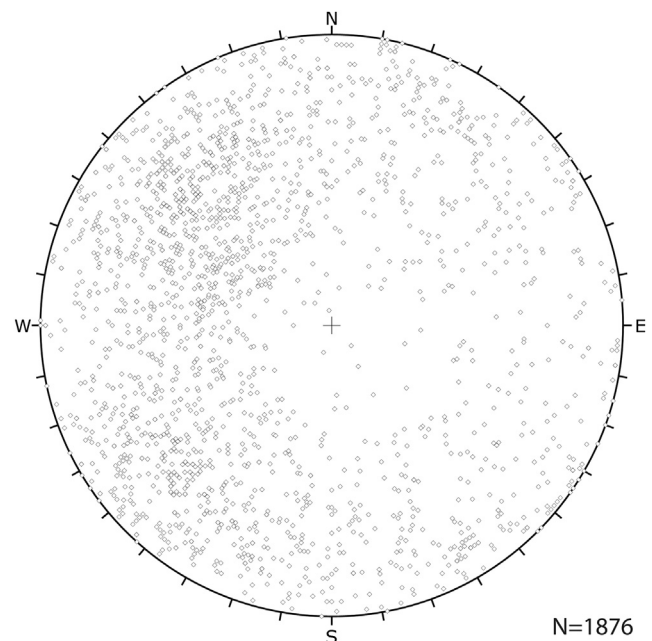

Fig. A1. Stereoplot of poles to discontinuities calculated from photogrammetry for all photograph locations (no contouring).
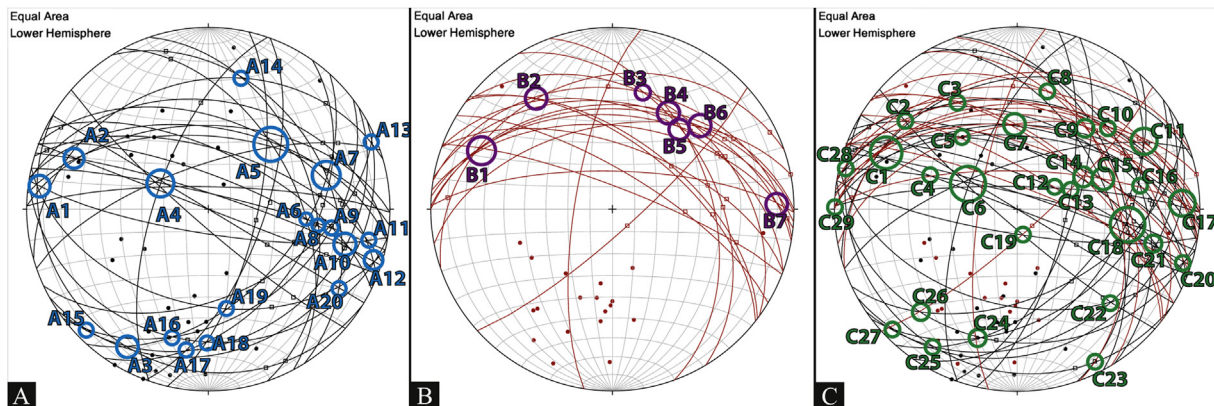
Appendix B

Fig. B1. (A)–(C) Stereoplots of *M*-planes of slickenside plane and lineation data collected by hand compass. Great circles are *M*-planes, hollow squares are slickenside lineations, and solid dots are poles to great circles (π*M*-points). Terminology is after Aleksandrowski (1985). (A) Data from mineralized slickenfibers. Blue circles are common intersection points (CIPs) of *M*-planes analyzed in this study. (B) Data from unmineralized slickenlines. Purple circles are CIPs examined in this study. (C) Combination of both slickenfiber (black) and slickenline (red) data from A and B, respectively. Green circles are CIPs of both types of slickenfibers examined in this study. Results shown in Fig. 12. (For interpretation of the references to color in this figure legend, the reader is referred to the web version of this article.)

References

Adams, C.J.D., 1975. Discovery of Precambrian rocks in New Zealand: age relations of the Greenland Group and constant gneiss, West Coast, South Island. Earth and Planetary Science Letters 28, 98–104.

Adams, J., 1980. Paleoseismicity of the Alpine Fault seismic gap, New Zealand. Geology 8, 72–76.

Adams, C.J., 2004. Rb–Sr age and strontium isotope characteristics of the Greenland Group, Buller Terrane, New Zealand, and correlations at the East Gondwanaland margin. New Zealand Journal of Geology and Geophysics 47, 189–200.

Aleksandrowski, P., 1985. Graphical determination of principal stress directions for slickenside lineation populations: an attempt to modify Arthaud's method. Journal of Structural Geology 7 (1), 73–82.

Anderson, E.M., 1951. The Dynamics of Faulting, second ed. Oliver and Boyd, Edinburgh.

Anderson, H., Webb, T., Jackson, J., 1993. Focal mechanisms of large earthquakes in the South Island of New Zealand: implications for the accommodation of Pacific–Australia plate motion. Geophysical Journal International 115, 1032–1054.

Arthaud, F., 1969. Méthode de détermination graphique des directions de raccourcissement, d'allongement et intermédiaire d'une population de failles. Bulletin de la Société Géologique de France 7 (11), 729–737.

Barth, N.C., Toy, V.G., Langridge, R.M., Norris, R.J., 2012. Scale dependence of oblique plate-boundary partitioning: new insights from LiDAR, central Alpine Fault, New Zealand. Lithosphere 4 (5), 435–448. http://dx.doi.org/10.1130/L201.1.

Beavan, J., Ellis, S., Wallace, L., Denys, P., 2007. Kinematic constraints from GPS on oblique convergence of the Pacific and Australian Plates, central South Island, New Zealand. In: Okaya, D., Stern, T., Davey, F. (Eds.), A Continental Plate Boundary: Tectonics at South Island, New Zealand, AGU Geophysical Monograph Series, vol. 175, pp. 75–94. http://dx.doi.org/10.1029/175GM05.

Beavan, J., Haines, J., 2001. Contemporary horizontal velocity and strain rate fields of the Pacific–Australian plate boundary zone through New Zealand. Journal of Geophysical Research 106 (B1), 741–770.

Ben-Zion, Y., Shi, Z., 2005. Dynamic rupture on a material interface with spontaneous generation of plastic strain in the bulk. Earth and Planetary Science Letters 236, 486–496.

Berryman, K.R., Cochran, U.A., Clark, K.J., Biasi, G.P., Langridge, R.M., Villamor, P., 2012. Major earthquakes occur regularly on an isolated plate boundary fault. Science 336, 1690–1693.

Boutareaud, S., Wibberley, C.A.J., Fabbri, O., Shimamoto, T., 2008. Permeability structure and co-seismic thermal pressurization on fault branches: insights from the Usukidani fault, Japan. In: Wibberley, C.A.J., Kurz, W., Imber, J., Holdsworth, R.E., Collettini, C. (Eds.), The Internal Structure of Fault Zones: Implications for Mechanical and Fluid-Flow Properties, Geological Society, London, Special Publications, vol. 299, pp. 341–361. http://dx.doi.org/10.1144/SP299.20.

Brideau, M.-A., Sturzenegger, M., Stead, D., Jaboyedoff, M., Lawrence, M., Roberts, M., Ward, B., Millard, T., Clague, J., 2012. Stability analysis of the 2007 Chehalis lake landslide based on long-range terrestrial photogrammetry and airborne LiDAR data. Landslides 9, 75–91. http://dx.doi.org/10.1007/s10346-011-0286-4.

Bruhn, R.L., Yusas, M.R., Huertas, F., 1982. Mechanics of low-angle normal faulting: an example from Roosevelt Hot Springs geothermal area, Utah. Tectonophysics 86, 343–361.

Caine, J.S., Evans, J.P., Forster, C.B., 1996. Fault zone architecture and permeability structure. Geology 24 (11), 1025–1028.

Caine, J.S., Bruhn, R.L., Forster, C.B., 2010. Internal structure, fault rocks, and inferences regarding deformation, fluid flow, and mineralization in the seismogenic Stillwater normal fault, Dixie Valley, Nevada. Journal of Structural Geology 32, 1576–1589.

Chester, F.M., Chester, J.S., 1998. Ultracataclasite structure and friction processes of the Punchbowl fault, San Andreas system, California. Tectonophysics 295, 199–221.

Chester, F.M., Evans, J.P., Biegel, R.L., 1993. Internal structure and weakening mechanisms of the San Andreas Fault. Journal of Geophysical Research 98 (B1), 771–786.

Chester, F.M., Logan, J.M., 1987. Composite planar fabric of gouge from the Punchbowl Fault, California. Journal of Structural Geology 9 (5/6), 621–634.

Cooper, A.F., Norris, R.J., 1994. Anatomy, structural evolution, and slip rate of a plate-boundary thrust: the Alpine Fault at Gaunt Creek, Westland, New Zealand. Geological Society of America Bulletin 106, 627–633.

Cooper, R.A., Tulloch, A.J., 1992. Early Palaeozoic terranes in New Zealand and their relationship to the Lachlan Fold Belt. Tectonophysics 214, 129–144.

Cox, S.C., Barrell, D.J.A., 2007. Geology of the Aoraki Area. Institute of Geological and Nuclear Sciences. Geological map 15, scale 1:250,000.

Craw, D., Campbell, J.R., 2004. Tectonic and structural setting for active and mesothermal gold vein systems, Southern Alps, New Zealand. Journal of Structural Geology 26, 995–1005.

CSIRO (Commonwealth Scientific and Industrial Research Organisation), 2010. Siro3D, Sirovision 3D Imaging Mapping System Manual. Version 4.1.

Davey, F.J., Henyey, T., Kelffmann, S., Melhuish, A., Okaya, D., Stern, T.A., Woodward, D.J., 1995. Crustal reflections from the Alpine Fault Zone, South Island, New Zealand. New Zealand Journal of Geology and Geophysics 38, 601–604.

De Pascale, G.P., Langridge, R.M., 2012. New on-fault evidence for a great earthquake in A.D. 1717, central Alpine Fault, New Zealand. Geology 40 (9), 791–794.

De Ronde, C.E.J., Sibson, R.H., Bray, C.J., Faure, K., 2001. Fluid chemistry of veining associated with an ancient microearthquake swarm, Benmore Dam, New Zealand. GSA Bulletin 113 (8), 1010–1024.

DeMets, C., Gordon, R.G., Argus, D.F., Stein, S., 1994. Effect of recent revisions to the geomagnetic reversal time scale on estimates of current plate motions. Geophysical Research Letters 21 (20), 2191–2194.

Dor, O., Rockwell, T.K., Ben-Zion, Y., 2006. Geological observations of damage asymmetry in the structure of the San Jacinto, San Andreas and Punchbowl faults in Southern California: a possible indicator for preferred rupture propagation direction. Pure and Applied Geophysics 163, 301–349.

Dor, O., Yildirim, C., Rockwell, T.K., Ben-Zion, Y., Emre, O., Sisk, M., Duman, T.Y., 2008. Geological and geomorphologic asymmetry across the rupture zones of the 1943 and 1944 earthquakes on the North Anatolian Fault: possible signals for preferred earthquake propagation direction. Geophysical Journal International 173, 483–504.

Evison, F.F., 1971. Seismicity of the Alpine Fault, New Zealand. In: Collins, B.W., Fraser, R. (Eds.), Recent Crustal Movements, Royal Society of New Zealand Bulletin, vol. 9, pp. 161–165.

Faulkner, D.R., Jackson, C.A.L., Lunn, R.J., Schlische, R.W., Shipton, Z.K., Wibberley, C.A.J., Withjack, M.O., 2010. A review of recent developments concerning the structure, mechanics, and fluid properties of fault zones. Journal of Structural Geology 32, 1557–1575.

Faulkner, D.R., Mitchell, T.M., Healy, D., Heap, M.J., 2006. Slip on 'weak' faults by the rotation of regional stress in the fracture damage zone. Nature 444, 922–925.

Faulkner, D.R., Mitchell, T.M., Rutter, E.H., Cembrano, J., 2008. On the structure and mechanical properties of large strike-slip faults. In: Wibberley, C.A.J., Kurz, W., Imber, J., Holdsworth, R.E., Collettini, C. (Eds.), The Internal Structure of Fault Zones: Implications for Mechanical and Fluid-Flow Properties, Geological Society, London, Special Publications, vol. 299, pp. 139–150. http://dx.doi.org/10.1144/SP299.9.

Ferrill, D.A., Smart, K.J., Necsiou, M., 2008. Displacement-length scaling for single-event fault ruptures: insights from Newberry Springs Fault Zone and implications for fault zone structure. In: Wibberley, C.A.J., Kurz, W., Imber, J., Holdsworth, R.E., Collettini, C. (Eds.), The Internal Structure of Fault Zones: Implications for Mechanical and Fluid-Flow Properties, Geological Society, London, Special Publications, vol. 299, pp. 113–122.

Finzi, Y., Hearn, E.H., Ben-Zion, Y., Lyakhovsky, V., 2009. Structural properties and deformation patterns of evolving strike-slip faults: numerical simulations incorporating damage rheology. Pure and Applied Geophysics 166, 1537–1573.

Fisher, N.I., Lewis, T., Embleton, B.J.J., 1987. Statistical Analysis of Spherical Data. Cambridge University Press, Cambridge.

Haneberg, W.C., 2008. Using close range terrestrial digital photogrammetry for 3-D rock slope modeling and discontinuity mapping in the United States. Bulletin of Engineering Geology and the Environment 67, 457–469. http://dx.doi.org/10.1007/s10064-008-0157-y.

Haxby, W.F., Melkonian, A.K., Coplan, J., Chan, S.-M., Ryan, W.B.F., 2010. Geo-MapApp Freeware Software. v.2.3. Lamont– Doherty Earth Observatory, Palisades, NY.

Hill, D.P., 1977. A model for earthquake swarms. Journal of Geophysical Research 82 (8), 1347–1352.

Howarth, J.D., Fitzsimons, S.J., Norris, R.J., Jacobsen, G.E., 2012. Lake sediments record cycles of sediment flux driven by large earthquakes on the Alpine Fault, New Zealand. Geology 40, 1091–1094.

Ikesawa, E., Sakaguchi, A., Kimura, G., 2003. Pseudotachylyte from an ancient accretionary complex: evidence for melt generation during seismic slip along a master décollement? Geology 31 (7), 637–640.

Ireland, T.R., 1992. Crustal evolution of New Zealand: evidence from age distributions of detrital zircons in Western Province paragneisses and Torlesse greywacke. Geochimica et Cosmochimica Acta 56, 911–920.

Kamb, W.B., 1959. Ice petrofabric observations from Blue Glacier, Washington, relation to theory and experiment. Journal of Geophysical Research 64 (11), 1891–1909.

Kamp, P.J.J., Green, P.F., Tippett, J.M., 1992. Tectonic architecture of the mountain front-foreland basin transition, South Island, New Zealand, assessed by fission track analysis. Tectonics 11 (1), 98–113.

Kassem, O.K., Ring, U., 2004. Underplating-related finite-strain patterns in the Gran Paradiso massif, Western Alps, Italy: heterogeneous ductile strain superimposed on a nappe stack. Journal of the Geological Society, London 161, 875–884.

Lato, M.J., Diedrichs, M.S., Hutchinson, D.J., 2010. Bias correction for view-limited Lidar scanning of rock outcrops for structural characterization. Rock Mechanics and Rock Engineering 43, 615–628. http://dx.doi.org/10.1007/s00603-010-0086-5.

Leitner, B., Eberhart-Phillips, D., Anderson, H., Nabelek, J.L., 2001. A focused look at the Alpine Fault, New Zealand: seismicity, focal mechanisms, and stress observations. Journal of Geophysical Research 106 (B2), 2193–2220.

Little, T.A., Cox, S., Vry, J.K., Batt, G., 2005. Variations in exhumation level and uplift rate along the oblique-slip Alpine Fault, central Southern Alps, New Zealand. Geological Society of America Bulletin 117 (5/6), 707–723.

Little, T.A., Holcombe, R.J., Ilg, B.R., 2002. Ductile fabrics in the zone of active oblique convergence near the Alpine Fault, New Zealand: identifying the neotectonic overprint. Journal of Structural Geology 24, 193–217.

Meneghini, F., Moore, J.C., 2007. Deformation and hydrofracture in a subduction thrust at seismogenic depths: the Rodeo Cove thrust zone, Marin Headlands, California. Geological Society of America Bulletin 119 (1/2), 174–183.

Micarelli, L., Benedicto, A., Wibberley, C.A.J., 2006. Structural evolution and permeability of normal fault zones in highly porous carbonate rocks. Journal of Structural Geology 28, 1214–1227.

Mitchell, T.M., Ben-Zion, Y., Shimamoto, T., 2011. Pulverized fault rocks and damage asymmetry along the Arima-Takatsuki Tectonic Line, Japan. Earth and Planetary Science Letters 308, 284–297.

Mitchell, T.M., Faulkner, D.R., 2009. The nature and origin of off-fault damage surrounding strike-slip fault zones with a wide range of displacements: a field study from the Atacama fault system, northern Chile. Journal of Structural Geology 31, 802–816.

Moore, D.E., Lockner, D.A., Byerlee, J.D., 1994. Reduction in permeability in granite at elevated temperatures. Science 265 (5178), 1558–1561.

Nathan, S., Thurlow, C., Warnes, P., Zucchetto, R., 2000. Geochronology Database for New Zealand Rocks (2nd ed.): 1961–1999. In: Institute of Geological & Nuclear Sciences Reports Series 5, 2000/11.

Norris, R.J., Koons, P.O., Cooper, A.F., 1990. The obliquely-convergent plate boundary in the South Island of New Zealand: implications for ancient collision zones. Journal of Structural Geology 12 (5/6), 715–725.

Norris, R.J., Cooper, A.F., 1986. Small-scale fractures, glaciated surfaces, and recent strain adjacent to the Alpine Fault, New Zealand. Geology 14, 687–690.

Norris, R.J., Cooper, A.F., 1995. Origin of small-scale segmentation and transpressional thrusting along the Alpine Fault, New Zealand. GSA Bulletin 107 (2), 231–240.

Norris, R.J., Cooper, A.F., 1997. Erosional control on the structural evolution of a transpressional thrust complex on the Alpine Fault, New Zealand. Journal of Structural Geology 19 (10), 1323–1342.

Norris, R.J., Cooper, A.F., 2001. Late Quaternary slip rates and slip partitioning on the Alpine Fault, New Zealand. Journal of Structural Geology 23, 507–520.

Norris, R.J., Cooper, A.F., 2007. The Alpine Fault, New Zealand: surface geology and field relationships. In: Okaya, D., Stern, T., Davey, F. (Eds.), A Continental Plate Boundary: Tectonics at South Island, New Zealand, American Geophysical Union Geophysical Monograph Series, vol. 175, pp. 157–175.

Oliver, N.H.S., Bons, P.D., 2001. Mechanisms of fluid flow and fluid-rock interaction in fossil metamorphic hydrothermal systems inferred from vein-wallrock patters, geometry, and microstructure. Geofluids 1, 137–162.

Passchier, C.W., 2008. Photograph of the month. Journal of Structural Geology 30 (1), 1. http://dx.doi.org/10.1016/j.jsg.2007.07.001.

Peacock, D.C.P., Sanderson, D.J., 1992. Effects of layering and anisotropy on fault geometry. Journal of the Geological Society, London 194, 793–802.

Pearson, C., Denys, P., Hodgkinson, K., 2000. Geodetic constraints on the kinematics of the Alpine Fault in the southern South Island of New Zealand, using results from the Hawea-Haast GPS transect. Geophysical Research Letters 27 (9), 1319–1322.

Phillips, C.J., Cooper, A.F., Palin, J.M., Nathan, S., 2005. Geochronological constraints on Cretaceous–Paleocene volcanism in South Westland, New Zealand. New Zealand Journal of Geology and Geophysics 48, 1–14.

Ramsay, J.G., 1980. Shear zone geometry: a review. Journal of Structural Geology 2 (1/2), 83–99.

Rattenbury, M.S., 1991. The Fraser Complex: high-grade metamorphic, igneous, and mylonitic rocks in central Westland, New Zealand. New Zealand Journal of Geology and Geophysics 34, 23–33.

Rawling, G.C., Goodwin, L.B., Wilson, J.B., 2001. Internal architecture, permeability structure, and hydrologic significance of contrasting fault-zone types. Geology 29 (1), 43–46.

Reinen, L.A., 2000. Seismic and aseismic slip indicators in serpentinite gouge. Geology 28 (2), 135–138.

Ridley, J., 1993. The relations between mean rock stress and fluid flow in the crust: with reference to vein- and lode-style gold deposits. Ore Geology Reviews 8, 23–37.

Rockwell, T., Ben-Zion, Y., 2007. High localization of primary slip zones in large earthquakes from paleoseismic trenches: observations and implications for earthquake physics. Journal of Geophysical Research 112, B10304. http://dx.doi.org/10.1029/2006JB004764.

Rocscience, 2006. Dips. v.6.0. Rocscience, Toronto.

Ryan, W.B.F., Carbotte, S.M., Coplan, J.O., O'Hara, S., Melkonian, A., Arko, R., Wiessel, R.A., Ferrini, V., Goodwillie, A., Nitsche, F., Bonczkowski, J., Zemsky, R., 2009. Global multi-resolution topography synthesis. Geochemistry Geophysics Geosystems 10 (3), 1–9. http://dx.doi.org/10.1029/2008GC002332.

Sagy, A., Brodsky, E.E., 2009. Geometric and rheological asperities in an exposed fault zone. Journal of Geophysical Research 114, B02301. http://dx.doi.org/10:1029/2008JB005701.

Sagy, A., Brodsky, E.E., Axen, G.J., 2007. Evolution of fault-surface roughness with slip. Geology 35 (3), 283–286.

Scholz, C.H., 1998. Earthquakes and friction laws. Nature 391, 37–42.

Secor, D.T., 1965. Role of fluid pressure in jointing. American Journal of Science 263, 633–646.

Seward, D., Nathan, S., 1990. Uplift history of South Westland using the fission-track dating technique. New Zealand Journal of Geology and Geophysics 33, 201–204.

Sibson, R.H., 1977. Fault rocks and fault mechanisms. Journal of the Geological Society, London 133, 191–213.

Sibson, R.H., 1985. A note on fault reactivation. Journal of Structural Geology 7 (6), 751–754.

Sibson, R.H., 1990. Conditions for fault-valve behavior. In: Geological Society, London, Special Publications, vol. 54, pp. 15–28.

Sibson, R.H., 1992. Implications of fault-valve behavior for rupture nucleation and recurrence. Tectonophysics 211, 283–293.

Sibson, R.H., 2000. A brittle failure mode plot defining conditions for high-flux flow. Economic Geology 95, 41–48.

Sibson, R.H., 2003. Brittle-failure controls on maximum sustainable overpressure in different tectonic regimes. AAPG Bulletin 87 (6), 901–908.

Sibson, R.H., Robert, F., Poulsen, K.H., 1988. High-angle reverse faults, fluid-pressure cycling, and mesothermal gold-quartz deposits. Geology 16, 551–555.

Sibson, R.H., Scott, J., 1998. Stress/fault controls on the containment and release of overpressured fluids: examples from gold-quartz vein systems in Juneau, Alaska; Victoria, Australia and Otago, New Zealand. Ore Geology Reviews 13, 293–306.

Sturzenegger, M., Stead, D., 2009. Close-range terrestrial digital photogrammetry and terrestrial laser scanning for discontinuity characterization on rock cuts. Engineering Geology 106, 163–182. http://dx.doi.org/10.1016/j.enggeo.2009.03.004.

Sutherland, R., 1996. Transpressional development of the Australia–Pacific boundary through southern South Island, New Zealand: constraints from Miocene–Pliocene sediments, Waiho-1 borehole, South Westland. New Zealand Journal of Geology and Geophysics 39, 251–264.

Sutherland, R., Berryman, K., Norris, R.J., 2006. Quaternary slip rate and geomorphology of the Alpine Fault: implications for kinematics and seismic hazard in southwest New Zealand. Geological Society of America Bulletin 118 (3/4), 464–474.

Sutherland, R., Davey, F., Beavan, J., 2000. Plate boundary deformation in South Island, New Zealand, is related to inherited lithospheric structure. Earth and Planetary Science Letters 177, 141–151.

Sutherland, R., Eberhart-Phillips, D., Harris, R.A., Stern, T., Beavan, J., Ellis, S., Henrys, S., Cox, S., Norris, R.J., Berryman, K.R., Townend, J., Bannister, S., Pettinga, J., Leitner, B., Wallace, L., Little, T.A., Cooper, A.F., Yetton, M., Stirling, M., 2007. Do great earthquakes occur on the Alpine Fault in central South Island, New Zealand. American Geophysical Union, Geophysical Monograph 175, 235–251.

Sutherland, R., Toy, V.G., Townend, J., Cox, S.C., Eccles, J.D., Faulkner, D.R., Prior, D.J., Norris, R.J., Mariani, E., Boulton, C., Carpenter, B.M., Menzies, C.D., Little, T.A., Hasting, M., De Pascale, G.P., Langridge, R.M., Scott, H.R., Reid Lindroos, Z., Fleming, B., Kopf, A.J., 2012. Drilling reveals fluid control on architecture and rupture of the Alpine Fault, New Zealand. Geology 40 (12), 1143–1146. http://dx.doi.org/10.1130/G33614.1.

Templeton, E.L., Rice, J.R., 2006. Extent and distribution of off-fault plasticity during seismic rupture including bimaterial effects. In: American Geophysical Union Fall Meeting 2006. abstract #S34A-01.

Templeton, E.L., Rice, J.R., 2008. Off-fault plasticity and earthquake rupture dynamics: 1. Dry materials or neglect of fluid pressure changes. Journal of Geophysical Research 113, B09306. http://dx.doi.org/10.1029/2007JB005529.

Tenthorey, E., Cox, S.F., Todd, H.F., 2003. Evolution of strength recovery and permeability during fluid-rock reaction in experimental fault zones. Earth and Planetary Science Letters 206, 161–172.

Terzaghi, R.D., 1965. Sources of error in joint surveys. Geotechnique 15, 287–304.

Townend, J., Sherburn, S., Arnold, R., Boese, C., Woods, L., 2012. Three-dimensional variations in present-day tectonic stress along the Australia–Pacific plate boundary in New Zealand. Earth and Planetary Science Letters 353–354, 47–59.

Toy, V.G., Prior, D.J., Norris, R.J., 2008. Quartz fabrics in the Alpine Fault mylonites: influence of pre-existing preferred orientations on fabric development during progressive uplift. Journal of Structural Geology 30, 602–621.

Tulloch, A.J., Ramezani, J., Mortimer, N., Mortensen, J., van den Bogaard, P., Maas, R., 2009. Cretaceous felsic volcanism in New Zealand and Lord Howe Rise (Zealandia) as a precursor to final Gondwana break-up. In: Ring, U., Wernicke, B. (Eds.), Extending a Continent: Architecture, Rheology and Heat Budget, Geological Society of London Special Publication, vol. 321, pp. 89–118.

Twiss, R.J., Gefell, M.J., 1990. Curved slickenfibers: a new brittle shear sense indicator with application to a sheared serpentinite. Journal of Structural Geology 12 (4), 471–481.

Van der Pluijm, B.A., Marshak, S., 2004. Earth Structure: An Introduction to Structural Geology and Tectonics, second ed. W. W. Norton & Company, New York.

Walcott, R.I., 1978. Present tectonics and Late Cenozoic evolution of New Zealand. Geophysical Journal of the Royal Astronomical Society 52, 137–164.

Walcott, R.I., 1998. Modes of oblique compression: Late Cenozoic tectonics of the South Island of New Zealand. Reviews of Geophysics 36 (1), 1–26.

Wibberley, C.A.J., Shimamoto, T., 2003. Internal structure and permeability of major strike-slip fault zones: the Median Tectonic Line in Mie Prefecture, Southwest Japan. Journal of Structural Geology 25, 59–78.

Wibberley, C.A.J., Yielding, G., Di Toro, G., 2008. Recent advances in the understanding of fault zone internal structure: a review. In: Geological Society, London, Special Publications, vol. 299, pp. 5–33.

Wooding, A.C., 1984. The Geology of the Omoeroa Range and Canavans Knob. BSc (Hons) thesis. University of Otago.